Universidade Federal
do Rio de Janeiro
Escola Politécnica

DESENVOLVIMENTO E IMPLEMENTAÇÃO DO CONTROLE DE UMA MÃO ROBÓTICA DO TIPO MULTIFINGER

Gabriel Felippe da Cruz Pacheco

Projeto de Graduação apresentado ao Curso de Engenharia de Controle e Automação da Escola Politécnica, Universidade Federal do Rio de Janeiro, como parte dos requisitos necessários à obtenção do título de Engenheiro.

Orientador: Fernando Cesar Lizarralde

Rio de Janeiro
Dezembro de 2014

DESENVOLVIMENTO E IMPLEMENTAÇÃO DO CONTROLE DE UMA MÃO ROBÓTICA DO TIPO MULTIFINGER

Gabriel Felippe da Cruz Pacheco

PROJETO DE GRADUAÇÃO SUBMETIDO AO CORPO DOCENTE DO CURSO DE ENGENHARIA DE CONTROLE E AUTOMAÇÃO DA ESCOLA POLITÉCNICA DA UNIVERSIDADE FEDERAL DO RIO DE JANEIRO COMO PARTE DOS REQUISITOS NECESSÁRIOS PARA A OBTENÇÃO DO GRAU DE ENGENHEIRO DE CONTROLE E AUTOMAÇÃO.

Examinado por:

Prof. Fernando Cesar Lizarralde, D.Sc.

Prof. Alessandro Jacoud Peixoto, D.Sc.

Dr. Antonio Candea Leite, D.Sc.

RIO DE JANEIRO, RJ – BRASIL
DEZEMBRO DE 2014

Felippe da Cruz Pacheco, Gabriel

Desenvolvimento e implementação do controle de uma mão robótica do tipo multifinger/Gabriel Felippe da Cruz Pacheco. – Rio de Janeiro: UFRJ/Escola Politécnica, 2014.

XI, 65 p. : il. ; 29, 7cm.

Orientador: Fernando Cesar Lizarralde

Projeto de Graduação – UFRJ/ Escola Politécnica/ Curso de Engenharia de Controle e Automação, 2014.

Referências Bibliográficas: p. 62 – 65.

1. Robótica de manipulação. 2. Estimação de Forças de Contato. 3. Controle Robusto Descentralizado. 4. Síntese H_∞ . 5. Identificação e Caracterização de Sistemas.
I. Cesar Lizarralde, Fernando. II. Universidade Federal do Rio de Janeiro, Escola Politécnica, Curso de Engenharia de Controle e Automação. III. Título.

Acknowledgements

Primarily, I would like to wish my sincere thanks to my supervisor at CEA Mathieu Grossard for giving me the opportunity to work with him in the CEA Interactive Robotics Laboratory in such a huge project. I would like also to accentuate that he was always available for helping me with all types of questions related not only to the project but also to my professional career. Furthermore, I express my very great appreciation to Guillaume Hamon, Benoît Perrochon and Pascal Chambaud who have helped me a lot either explaining important subjects or repairing the breakages I have done (specially the fingers' tendons).

I am also particularly grateful for the assistance given by family, girlfriend and friends who were always by my side supporting me on my decisions and cheering my nights and weekends throughout all those year of study. Finally, I wish to thank to my UFRJ's supervisor, Fernando Lizarralde, for accepting to validate this internship work as my Undergraduate Project and for giving me all the necessary support so that the final result could be successful.

Resumo do Projeto de Graduação apresentado à ESCOLA POLITÉCNICA/UFRJ como parte dos requisitos necessários para a obtenção do grau de Engenheiro de Controle e Automação.

DESENVOLVIMENTO E IMPLEMENTAÇÃO DO CONTROLE DE UMA MÃO ROBÓTICA DO TIPO MULTIFINGER

Gabriel Felippe da Cruz Pacheco

Dezembro/2014

Orientador: Fernando Cesar Lizarralde

Curso: Engenharia de Controle e Automação

Este trabalho apresenta algoritmos de controle para a mão robótica do CEA LIST. Uma estratégia de estimação de força, baseada somente em sinais proprioceptivos, é desenvolvida bem como controladores robustos de posicionamento de alto desempenho são elaborados. Primeiramente, o enfoque é dado nos fundamentos da concepção mecatrônica de tal mão robótica. Em seguida, a abordagem modular utilizada simplifica a montagem do sistema completo e permite que os esforços sejam concentrados numa unidade básica que é replicada em todas as partes da mão. Além disso, uma concepção mecânica otimizada assegura o desacoplamento de eixos e ainda proporcionam reversibilidade ao longo de todo o mecanismo, incluindo atuadores e a transmissão do movimento para as juntas.

Baseado nisto, forças externas aplicadas aos dedos podem ser sentidas no nível motor e, devido à modularidade e ao desacoplamento dos eixos, controladores robustos monovariáveis podem ser implementados para cada eixo acionado. A combinação de um mecanismo altamente eficiente e de grande sensibilidade a forças externas, podendo utilizar leis de controle *sensorless* em torque e robustas em posicionamento contribuem para a melhoria das habilidades de manipulação robótica. Os resultados experimentais validam a abordagem adotada e evidenciam uma mão robótica altamente integrada, capaz de manipular vários tipos de objetos e de estimar forças de contato sem o auxílio de sensores de força externos.

Palavras-chave: Robótica, estratégias de estimação de força, controle robusto de posicionamento, identificação e caracterização de sistemas.

Abstract of Undergraduate Project presented to POLI/UFRJ as a partial fulfillment of the requirements for the degree of Automation and Control Engineer.

DEVELOPMENT AND IMPLEMENTATION OF THE CONTROL OF A MULTIFINGER TYPE ROBOTIC HAND

Gabriel Felippe da Cruz Pacheco

December/2014

Advisor: Fernando Cesar Lizarralde

Course: Automation and Control Engineering

This work presents control algorithms for the CEA LIST dexterous robotic hand. A force sensing strategy only based on proprioceptive signals is developed as well as robust position controllers for high performance in-hand manipulation. We primarily focus on the mechatronic design rationale of the robotic hand. Then, a modular approach simplifies the complex hand assembly and permits to concentrate efforts on one basic unit which is replicated throughout the hand. An optimized mechanical design of this unit assures decoupled axes and backdrivability through the whole mechanism, including actuators and transmission of movement to the joints.

Based on this feature, external forces applied to the finger can be sensed at the motor level and, thanks to modularity and decoupling, mono-variable robust controllers can be developed for each finger's DoF. Overall, this mechatronic design contributes to the improvement of manipulation skills of robotic hands, thanks to the combination of high performance mechanics, high sensitivity to external forces, torque control capability without using external force sensor and high performance robust position control. Experimental results confirm the validity of our design approach and provide a highly integrated hand capable of grasping various kinds of objects and of estimating contact forces without any external sensors.

Keywords: Robotics, force sensing strategies, robust position control, systems characterization and identification

Résumé du Projet de Fin d'Études presenté à POLI/UFRJ comme une partie des exigences pour l'obtention du diplôme d'Ingénieur.

DÉVELOPPEMENT ET IMPLÉMENTATION DU CONTRÔLE-COMMANDE D'UNE MAIN ROBOTISÉE DE TYPE MULTIFINGER

Gabriel Felippe da Cruz Pacheco

Décembre/2014

Encadrant: Fernando Cesar Lizarralde

Cursus: Automatisation et Commande des Systèmes

Cette étude présente des algorithmes de commande pour la main robotisée dextre du CEA LIST. Une stratégie d'estimation de force de contact ne basée que dans des signaux proprioceptifs est développée ainsi que des contrôleurs robustes pour la manipulation fine des objets dans la main. Focalisons, tout d'abord, dans la conception mécatronique de la main robotisée. Ensuite, une approche modulaire simplifie le montage de la structure complète et nous permet de nous concentrer dans l'unité de base qui est répliquée dans toute la main. Une conception mécanique optimisée de cette unité garanti un découplage des axes ainsi que la réversibilité mécanique tout au long du mécanisme, y compris les actionneurs et la transmission du mouvement jusqu'aux articulations.

A partir de cette caractéristique, forces externes appliquées dans le doigt peuvent être senties au niveau moteur et, dû à la modularité et au découplage des axes, contrôleurs robustes mono-variables peuvent être synthétisés pour chaque ddl d'un doigt . Globalement, une telle conception mécanique contribue pour amélioration des habilités de manipulation de mains robotiques, grâce à la combinaison d'une mécanique performante, la grande sensibilité aux forces externes, une commande en couple sans utilisation de capteurs de force externes et une commande robuste en position de haute performance. Les résultats expérimentaux valident notre approche de conception et offrent une main robotisée vraiment intégrée, capable de saisir plusieurs types d'objets et d'estimer forces de contact sans utiliser des capteurs externes.

Mots-clés : Robotique, estimation de force, commande robuste en position, caractérisation et identification des systèmes

Contents

List of Figures

Part I

Description of the Robotic System

Chapter 1

Introduction

This chapter intends to present the context within which this project was conducted. At first, the Handle European project will be presented, following a general description of its goals and presentation of some characteristics. At the end of this chapter a resume of the report organization is outlined.

1.1 The Handle Project

Developmental pathway towards autonomy and dexterity in robot in-hand manipulation. This is the full title of this huge European Project which involves nine industrial and academic partners. The project has successfully ended in February 2013.

Among these partners, UPMC [1] is the project coordinator and the Shadow Company and the CEA [2] LIST take an important role as the industrial developers of two artificial robotic hands (one by each organism).

As presented in HANDLE's official "Description of Work", this project "aims at understanding how humans perform the manipulation of objects in order to replicate grasping and skilled in-hand movements with an anthropomorphic artificial hand, and thereby move robot grippers from current best practice towards more autonomous, natural and effective articulated hands. This project will focus on technological developments and, in addition, on fundamental multidisciplinary research aspects in order to endow the proposed robotic hand with advanced perception capabilities, high level feedback control and elements of intelligence that allow recognition of objects and context, reasoning about actions and a high degree of recovery from failure during the execution of dexterous tasks".

Besides dexterity, anthropomorphism is necessary not only if we aim at the study of human manipulation but also if the interaction with human-oriented en-

1. Université Pierre et Marie Currie
2. Commissariat à l'Énergie Atomique et aux Énergies Alternatives

vironments is intended. Regarding prosthetic hands applications, anthropomorphism and texture are important factors. To do so, it is necessary of being able to estimate the contact force acting on the end-effector, and the most direct method is to use exteroceptive force information such as force sensing resistors [1], tactile sensor [2], combination of load cells and tactile sensors [3], force/torque-mounted sensors [4], etc. However, those are potentially expensive strategies and could compromise physical integration and generate compactness issues, especially if a certain level of anthropomorphism or a high number of degrees of freedom are also requested, which is the case for prosthetic applications.

Figure 1.1: CEA Robotic Hand

1.2 General Description

Figure 1.1 shows the CEA dexterous Hand. It has five fingers, integrated actuation as well as low-level control in an human-size hand and forearm. The mechatronic design of the new dexterous CEA hand exactly replicate the kinematics of the human hand, adding up 20 actuated degrees of freedom and 24 degrees of mobility. Understand, for degree of mobility, each possible movement of all joints, even if it is coupled to another one, and for degree of freedom the joints which move independently from the others.

Thus, each DoF [3] is driven by specially designed backdrivable actuators, achieving a fingertip force of $4.2N$, which is considerably less than a human fingertip can do[5] but it is normal conditions for in-hand manipulation [6]. It integrates

3. Degree(s) of Freedom

an interface with the ROS environment and it also embeds the miniaturized power boards and DSPs implementing the low-level control algorithms that can be either in position or torque.

(a) CEA hand (b) Shadow hand

Figure 1.2: Comparison between HANDLE project's robotic hands

The electronic power boards and the low-level controller are embedded in the forearm to facilitate the connection of the hand on any robotic arm, as imposed by an objective of the HANDLE project. In addition, the actuators are positioned in the palm reducing the complex cable routing, allowing less friction (instability phenomena in position) and more precise and smooth movements for dexterous in-hand manipulation. This factor is the main difference between the CEA and the Shadow hands, on the UK Company hand the actuators are positioned in the forearm (Fig. 1.2).

The maximum electric power consumption of the overall system (CEA Hand) is $168W$ and the total weight is $4.4kg$, which is obviously a lot heavier than a human hand ($0.350 - 0550kg$ on average) but with a very similar size.

Dexterity refers to the capability of changing the position and orientation of a manipulated object from a given reference configuration to a different one, arbitrarily chosen within the hand workspace. Dexterity is related to both the mechanical structure and the sensory apparatus of the robotic hand, and it is the most important indicator of its actual functionality [7–9]. Following this trend, several companies, research centers and universities have carried out research and development activities related to dynamics and kinematics modeling as well as control design of multi-fingered robotic hands [10, 11]. The most popular multifingered hands on the market are Barret, Kinova, Robotiq and Schunck hands. However just the last one presents a 5-finger structure as well as both Handle

project's hands shown in Figure 1.2.

In Figure 1.3 it is shown situations involving dexterous manipulation for the final version of the CEA hand.

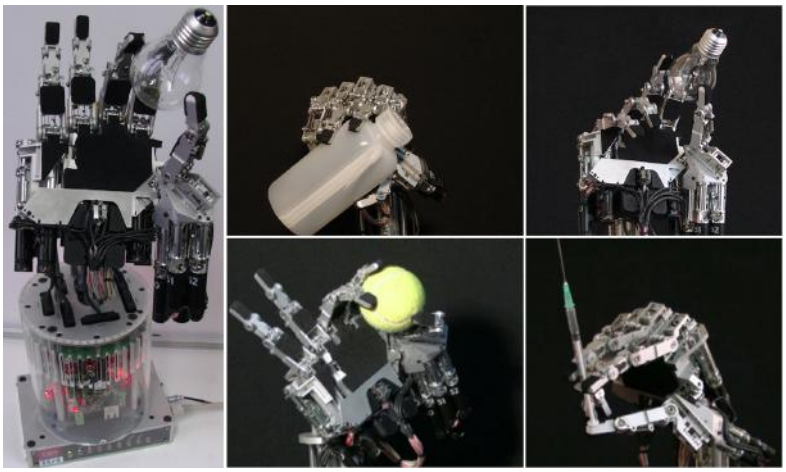

Figure 1.3: The CEA robotic hand used in the experiments [12].

1.3 Report Organization

At a first moment, in chapters 2 and 3 of part I, all the necessary assumptions and mathematical modeling are exposed so that, in parts II and III, the work done to achieve the main objectives of the project as well as some experimental results could be presented naturally. The final chapter, in part III, brings some final considerations with respect to the whole project and presents possible improvement points.

Detailing a bit more the tasks I was responsible for, we can state that the project was composed, basically, of two main objectives which will be presented in part II separate chapters.

1. Position and torque experiments for the CEA Robotic Hand;
2. Development and implementation of the low level decentralized robust controllers for each finger.

In the scope of the first goal, the position experiments lead us to prove the decoupling of the 3 axes unit (chapter 5) while the force ones, thanks to the backdrivability (section 2.3) of the ball-screw mechanisms, will allow us to develop a force-sensing algorithm using only the motor current information (chapter 4).

For the second objective, the modern control theory applied to robotic systems [13] and the H_∞ synthesis [14] permit the development of a multi-variable decentralized robust and high-performance controller for each finger (chapter 7) that, thanks to modularity (section 2.2), could be extended for all 5 fingers of the

CEA hand. Once the controllers are calculated, a phase of implementation comes and the digital controllers, or IIR [4] filters, are coded and embedded into the DSPs [5] that generate the PWM [6] signals for the DC [7] mini-motors bridges.

Regarding organization of the work load, the first part has been done from September 2012 until February 2013 while the second one has been performed from March 2013 until July 2013. Next chapter presents the details of the CEA hand kinematic that are necessary to build the complete mathematical model representing the system dynamics.

4. Infinity Impulse response
5. Digital Signal Processors
6. Pulse Width Modulation
7. Direct Current

Chapter 2

System Dynamics

In this chapter the mechanical design is briefly explained. Two key concepts have guided the mechanical design: **modularity** and **backdrivability**. These concepts will be explained in details throughout this chapter, but as a resume, modularity is the capacity of creating a base structure which will replicated all along the hand and backdrivability is the ability of a transmission to drive its input via its output. For an in-depth explanation of the design rationale and a detailed mathematical modeling, information can be found in [15] and [16].

2.1 Hand kinematics

When considering a large number of degrees of freedom, complex mechanics are more prone to bringing forward several disadvantages such as coupling between degrees of freedom, additional friction and backlash, non-desired compliance and complex dynamics that compromise the actual dexterity of the hand. Therefore, a careful design is required to minimize such disadvantages and provide a mechanical arrangement that enables a better controllability and thus an improved dexterity. The CEA dexterous Hand achieves a high level of anthropomorphism with 24 degrees of mobility which exactly replicate those of the human hand. It must be said that, even if the proposed kinematic structure seems to be similar to that of the Shadow Hand [17] both hands are completely different regarding actuation technology, tendon routing and in general design rationale. The complete kinematic structure of the hand can be summarized as follows:

- 4 degrees of mobility and 3 degrees of freedom per finger. The distal and intermediate phalanges are kinematically coupled with a constant ratio ;
- 5 degrees of freedom for the thumb ;
- 1 additional degree of freedom at the basis of the little finger ;
- 2 degrees of freedom for the wrist.

Such human hand kinematics is exclusively arranged with revolute pairs.

2.2 Modular Architecture

A modular approach has been taken which consists in focusing on the optimal solution of the *3 axes unit*. The 3-axes unit is a separable 3 Degrees of Freedom (DoF) sub-mechanism with which it is associated actuators, transmission and electronics unit, and it is common to all the fingers and the thumb (Fig. 2.1). It consists of a serial combination of abduction/adduction, flexion/extension and flexion/extension movements, where the axes of the abduction/adduction and the first flexion/extension intersect.

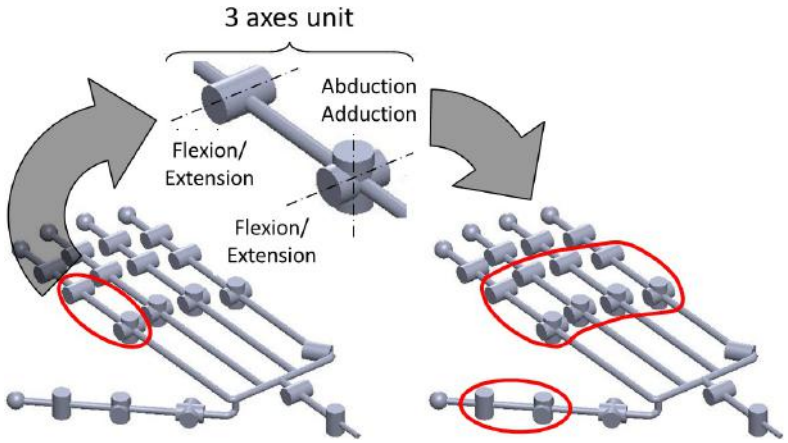

Figure 2.1: The modular approach in the context of the hand structure design.

A modular approach brings forward several advantages, such as simplification of the hand assembly, simplification of the hand maintenance, performance homogeneity and the possibility to have different hand configurations with different number of fingers or combination of fingers and thumb, for example.

2.3 Actuation and transmission

A key design feature of the 3 Axes Unit is the tendon routing, which minimizes the number of idle pulleys and direction changes in the cable routing, minimizing friction and thus maximizing backdrivability [18] related to the transmission.

Backdrivability is the ability of an actuator to have an interactive transmission of force/torque between the input and output axes [19]. In other words, a transmission is called backdrivable if a force or torque on its output can move its input. In order to achieve high backdrivability, friction of power transmission shall be reduced considerably. Backdrivable mechanisms have great force sensitivity and high impact resistance, which make them essential for human interactive robotics as it implies on flexibility. Figure 2.2 shows this two-way drive for a motor-link transmission.

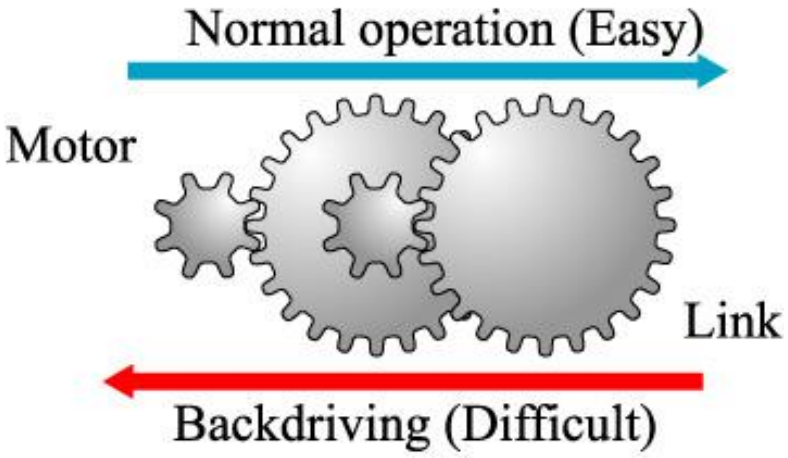

Figure 2.2: Two-way operation of a motor-link transmission [19]

For the actuation of the 20 DoF, backdrivable actuators have been specially designed, based on a rotary DC motor coupled to a ball-screw rotary-to-linear transmission. The induced displacement of the nut, which has been locked in rotation but left free to displace along its axis, is then transmitted to a tendon which finally drives a rotational joint. For high pitch-to-radius ratios, this actuator shows a good backdrivability. Backdrivability permits a single-acting actuation architecture with passive return, which greatly simplifies tendon routing and therefore reduces friction (note that friction associated with force transmitting tendons is by far the major source of friction in complex mechanical hands). Furthermore, overall backdrivability of the mechanism enables the measurement of external forces as a resistive torque induced on the DC motor shaft through the motor current sensing. This provides a measure of the contact forces.

Using a Steinmeyer Type B ball-screw of 3 mm diameter, 1 mm pitch p, and an integrated block-and-tackle mechanical amplification, an output force of 60 N has been achieved with a backdrivability threshold of 4 N at the actuator output. A linear position resolution of 0.001 mm is obtained by coupling a Maxon Encoder MR (Type M 512 cpt) to the motor. Two different versions of the actuator have been built: mono-directional to actuate the flexion/extension DoF in collaboration with passive return elements, and bi-directional to actuate the rest of DoF.

Finger assembly

The 3-axes unit consists of a serial combination of abduction/adduction (axis 1, angle q_1), flexion/extension (axis 2, angle q_2) and flexion/extension (axis 3, angle q_3), where axes 1 and 2 intersect. Axis 1 is driven with a double-acting actuation architecture and axes 2 and 3 are driven with a single-acting actuation architecture with passive return elements. All actuators are packed together upstream axis 1

and the movement is transmitted by tendons to all axes (Fig. 2.3).

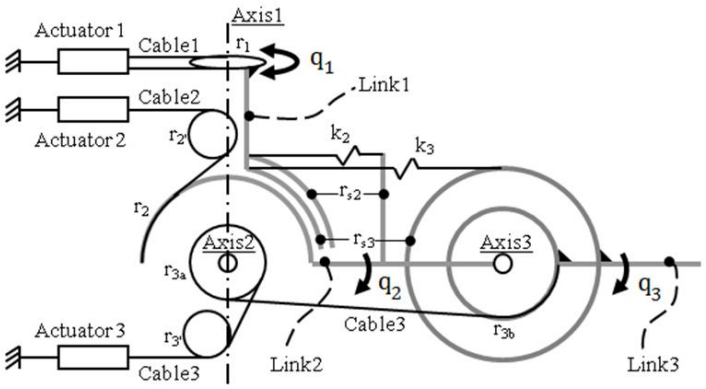

Figure 2.3: Schematic description of the 3-axes unit

Axis 1 is driven by Actuator 1 acting on pulley r_1 with Cable 1. Axis 2 is driven in the flexion movement by Actuator 2 acting on pulley r_2 with Cable 2, which passes trough idle pulley r'_2. The tangency point where Cable 2 leaves idle pulley r'_2 always lies on Axis 1. Axis 2 is driven in the extension movement by spring k_2. Spring k_2 is attached to link 1 by a cable which winds up on a pulley with radius r_{s2}, and is attached to link 2 at a vertical distance r_{s2}. Axis 3 is driven in the flexion movement by Actuator 3 acting on pulley r_{3b} with Cable 3, which passes trough idle pulleys r'_3 and r_{3a}. The tangency point where Cable 3 leaves idle pulley r'_3 always lies on Axis 1. Axis 3 is driven in the extension movement by spring k_3. Spring k_3 is attached to link 1 by a cable which winds up on a pulley with radius r_{s3}, and is attached to link 3 by a cable which winds up on a pulley with radius r_{s3}. The three actuators stay fixed. Pulleys r'_2, r'_3 and the portion of Cables 2, 3 connecting the actuators with pulleys r'_2, r'_3 stay always at the same plane. The rest of the mechanism (pulleys, cable portions and springs) is contained in a plane which pivots around Axis 1 by an angle q_1.

Such mechanical features prevents kinematic coupling due to the routing of springs nor static coupling due to reactions in the links between Abduction/Adduction movements and Flexion/Extension movements. No extra pulleys are needed to pass Cables 2, 3 through Axis 1 (which is a classical problem in tendon routing for mechanical hands), minimizing the number of idle pulleys and direction changes in the cable routing and, thereby, the overall amount of friction in the mechanism. A complete finger (Fig. 2.6) can be formed by a 3 Axes Unit plus an additional distal flexion $q_4 = cq_3$ which is mechanically coupled to axis 3. Such coupling consists in a constant ratio between the angles rotated by the last two phalanges. This results in a deterministic mechanism with 4 degrees of mobility and 3 degrees of freedom.

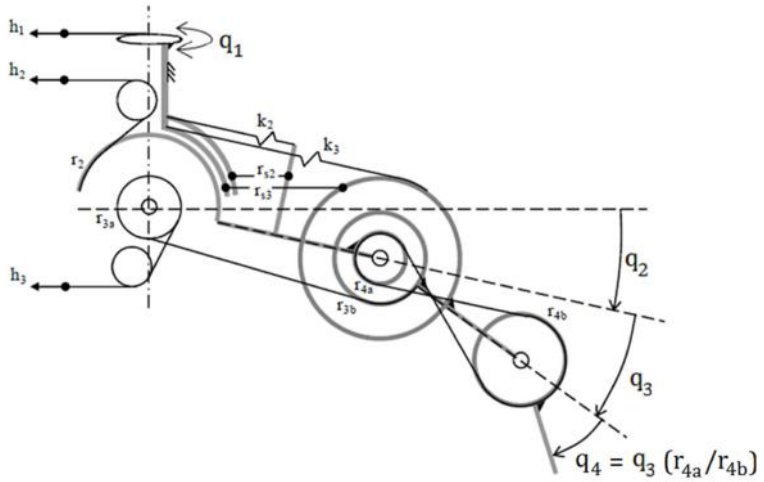

Figure 2.4: Tendon transmission connecting actuators with joints

As explained above, abduction/adduction movements are driven by bi-directional actuators while flexion/extension are driven by mono-directional actuators in collaboration with passive return elements.

In the following expressions, P is the coupling matrix for the tendon transmission, f is the vector of cable tensions, P_s is the coupling matrix for the passive return elements actuating on the joints, K is the stiffness matrix of the passive return elements, $e = \begin{bmatrix} 0 & e_{2,0} & e_{3,0} \end{bmatrix}^{\mathsf{T}}$ is the vector of initial extensions for the passive return elements, and $h_s(0) - h_s(q)$ is the vector of extension functions of the passive return elements. A detailed calculation of these elements is shown in [16]. All geometric parameters are optimized in order to maximize the force output of the 3 Axes Unit when integrated into the fingers, as well as the range of directions along which forces can be exerted taking into account the restriction given by $f_2, f_3 < 0$ (the cables related to the second and third actuators can only pull).

The routing of each tendon (figure 2.4) is modeled by an extension function which measures the displacement of the end of the tendon as a function of the finger's joint angles (positive when tendons are extended and negative when they are contracted). The vector of tendon extensions is given by:

$$h = \begin{bmatrix} l_{1,0} - r_1 q_1 \\ l_{2,0} - r_2 q_2 \\ l_{3,0} - r_{3a} q_2 - r_{3b} q_3 \end{bmatrix} \tag{2.1}$$

The coupling matrix is calculated as

$$P(q) = \frac{dh^{\mathsf{T}}}{dq} = \begin{bmatrix} -r_1 & 0 & 0 \\ 0 & -r_2 & -r_{3a} \\ 0 & 0 & -r_{3b} \end{bmatrix} \tag{2.2}$$

and using conservation of energy

$$\tau_{act} = P(q)\, f \tag{2.3}$$

Now, we will model the transmission of spring forces as elastic cables. The mechanism is detailed in figure 2.5. It is assumed that the tendons are completely free to slide along the pulleys of radius r_{s2} and r_{s3} in link 1 without friction. Hence we can lump all elasticity into a single spring element at the base of th tendon. Extensions functions are given by:

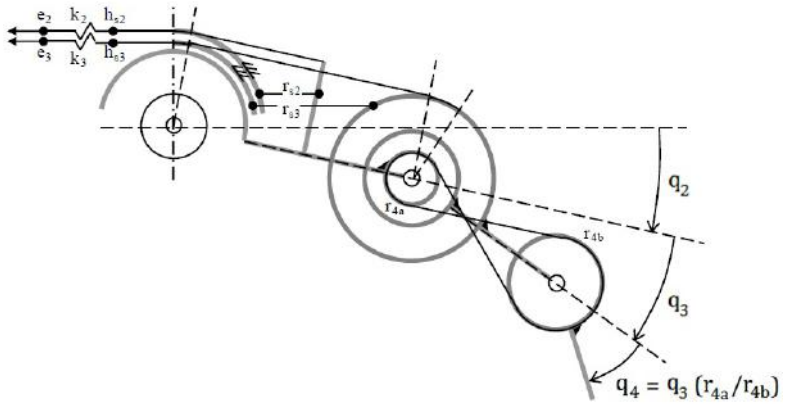

Figure 2.5: Tendon transmission connecting actuators with joints

$$h_s = \begin{bmatrix} 0 \\ l_{s2,0} + r_{s2} q_2 \\ l_{s3,0} + r_{s3} q_2 + r_{s3} q_3 \end{bmatrix} \tag{2.4}$$

The correspondent coupling matrix is calculated as

$$P_s(q) = \frac{dh_s^{\mathsf{T}}}{dq} = \begin{bmatrix} 0 & 0 & 0 \\ 0 & r_{s2} & r_{s3} \\ 0 & 0 & r_{s3} \end{bmatrix} \tag{2.5}$$

And the stiffness matrix is calculated as

$$K = \begin{bmatrix} 0 & 0 & 0 \\ 0 & k_2 & 0 \\ 0 & 0 & k_3 \end{bmatrix} \tag{2.6}$$

So the elongation of the tendons is given by

$$h_s(q) - h_s(0) = \underbrace{\begin{bmatrix} 0 & 0 & 0 \\ 0 & r_{s2} & 0 \\ 0 & r_{s3} & r_{s3} \end{bmatrix}}_{\Delta h_s} \begin{bmatrix} q_1 \\ q_2 \\ q_3 \end{bmatrix} \tag{2.7}$$

Finally, superposing the effects of actuator forces and spring forces, the net joint torques τ are given by [20]

$$\tau\left(q\right) = Pf + P_s\left(K\left(e + h_s\left(0\right) - h_s\left(q\right)\right)\right) \tag{2.8}$$

Considering that the springs are not initially extended or compressed ($e = 0$) , the previous equation can be simplified as follows:

$$\tau\left(q\right) = Pf - P_s K \Delta h_s q \tag{2.9}$$

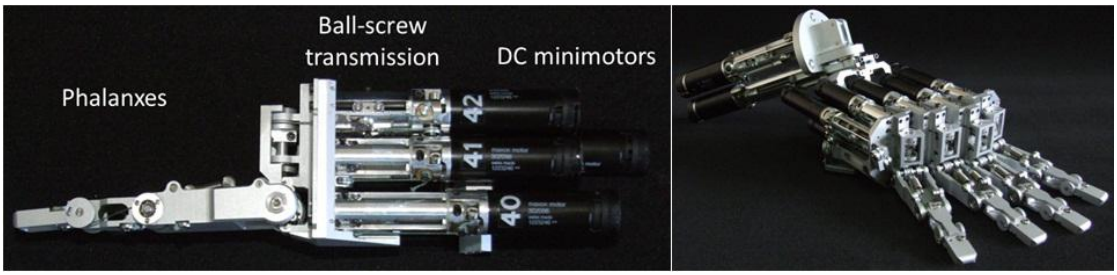

Figure 2.6: On the left: prototype of the 3-axes unit. On the right: assembly of the fingers, all fingers actuators being integrated in the palm.

2.4 Fingers dynamic equations

First, we consider the dynamic equation at the joint level. The values of the inertia, Coriolis and gravity matrices are all known and their calculation is detailed on the mathematical model presented in [15, 16]. Then the actuators dynamics is reflected on the joint level in order to obtain the final dynamic equation for the 3-axes unit.

$$M(q)\,\ddot{q} + C(q,\dot{q})\,\dot{q} + N(q) = \tau(q) \tag{2.10}$$

Using equations 2.7, 2.9 and 2.10 the following can be stated:

$$M(q)\,\ddot{q} + C(q,\dot{q})\,\dot{q} + P_s K \Delta h_s\, q + G(q) = P\, f \tag{2.11}$$

On the other hand, at the motor level the dynamic equation for the DC motors is:

$$J_m\,\ddot{\theta} + B_m\,\dot{\theta} = K_{em} i_m - \tau_{res} \tag{2.12}$$

where,

J_m : $diag(J_{m_i})$ with J_{m_i} the i-th motor inertia
B_m : $diag(b_{m_i})$ with b_{m_i} the i-th motor damping ratio
K_{em} : $diag(k_{m_i})$ with k_{m_i} the i-th motor electromagnetic constant
τ_{res} : Resistive torque applied by the tendons
i_m : Motor currents vector $[i_1\ i_2\ i_3]^\mathsf{T}$

At this point, it is necessary to find the relation between the motor (θ) and articular (q) variables. The kinematic relationship between the motors' rotation θ and the linear displacements h of the end tendon at the actuator output is given by $h = R\,\theta$, where R is the reduction ratio diagonal matrix. Also, using 2.2 we can write:

$$d\theta = \underbrace{R^{-1}P^\mathsf{T}}_{T}\,dq \tag{2.13}$$

where T is the transformation matrix from joint angles to motor ones. Applying the principle of energy conservation to the ball-screw mechanism, we have:

$$\tau_{res} = R\,f \;\;\Rightarrow\;\; P\,f = PR^{-1}\,\tau_{res} \tag{2.14}$$

Finally, combining equations 2.11, 2.12, 2.13 and 2.14 we can write the complete non-linear dynamic equation at the joint level for a finger as follows:

$$\boxed{\widetilde{M}(q)\,\ddot{q} + \widetilde{C}(q,\dot{q})\,\dot{q} + \widetilde{K}\,q + N(q) = T^\mathsf{T} K_{em}\,i_m} \tag{2.15}$$

where,

$$\begin{aligned} \widetilde{M}(q) &= M(q) + T^\mathsf{T} J_m T \\ \widetilde{C}(q,\dot{q}) &= C(q,\dot{q}) + T^\mathsf{T} B_m T \\ \widetilde{K} &= P_s K \Delta h_s \end{aligned} \tag{2.16}$$

This being shown, next chapter presents a complementary part of this project which is necessary to understand the work undertaken and the achieved results presented on parts II and III, respectively. It concerns the embedded electronics used to drive motors (and axes in consequence) and to interface the robot with a host-PC.

Chapter 3

Embedded Electronics & Control System

In this chapter the electronic architecture will be briefly discussed in order to give the reader a general idea of how the complete robotic hand is controlled. After that, the already implemented classical controllers are presented as well as the communication network and protocols. Also, a simple interface developed at the host in MATLAB/Simulink and its functionalities and limitations are commented.

3.1 Electronic Architecture

Following the modular mechanical design rationale of the hand, each 3 Axes Unit is controlled with an independent and integrated electronic architecture combining the low-level control part and power board, allowing position and torque control modes for each joint (Fig. 3.1).

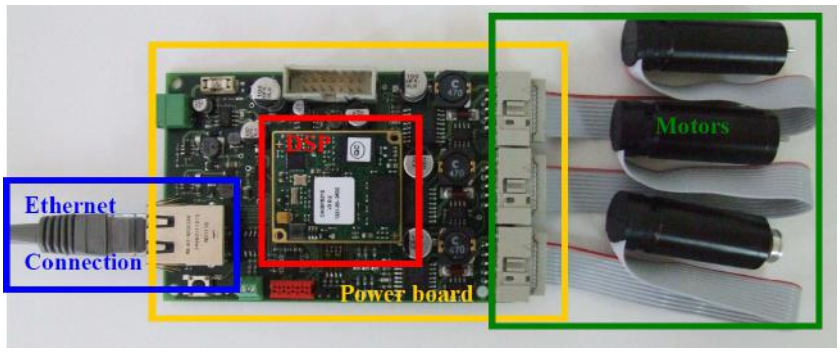

Figure 3.1: Elementary embedded electronic board with its main modules and the controlled mini DC-motors

Electronics have been designed to be embedded inside the robotic forearm so as to minimize wires and connectors to achieve a truly autonomous hand that can easily be connected to a robotic arm. The external wires have been limited

to the communication and power buses. This hardware includes power electronics, sensor interfaces, power supply, communication and Digital Signal Processors from Analog Device with an embedded Blackfin BF537 that can process the low level control of the hand and provide an external PC with all the data at a high communication rate. The DSP [1] uses a 32-bit fixed point controller with on-board memory. The CPU operates at 600 MHz and supports peripherals suitable for soft real-time control tasks, sech as event manager modules, several I/O ports, as well as 32-bit timer/counters with PWM capabilities. It also performs calculations for the three inner torque control loops.

The placement of the different components on the electronic board has been optimized to minimize the overall dimensions of the board ($100 \times 65 \times 15$ mm). Each power board embeds the three full bridges for the PWM generations, three units for measuring position of each motor encoder, ADC for the three current measurements and conversions, one Ethernet entry, one power supply and one DSP. The system architecture overview of one electronic board is described in Figure 3.2.

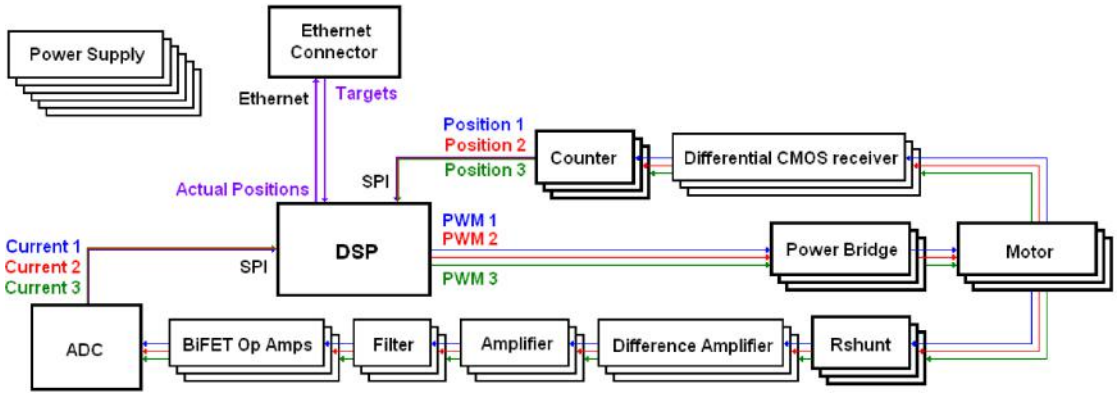

Figure 3.2: An electronic board for the control of the three motors of a 3-Axes Unit

Complementing the first 15 active degrees of freedom with the 5 active extra degrees relating to the thumb, the palm and the wrist, the future hand comprises a minimal number of 7 embedded DSPs to perform the control of the whole system. The host-PC communicates with the DSPs using a TCP/IP network architecture. Since the application needs, at least, soft real-time constraints, the UDP [2] protocol for the transport layer was preferable in comparison to TCP due to its significantly lower overhead (there are no acknowledges or handshakes features) and then it has a higher bandwidth. Surely a communication protocol based on the UDP iis not the best fit for hard real-time tasks since it is not deterministic on its principle and packets may be lost. However, as the applications did not involve significant

1. Digital Signal Processor
2. User Datagram Protocol

losses for a deadline miss, UDP has shown itself as a good choice for the project purposes. Within the network, the switch and the host-PC have fixed IPs and each port of the switch is connected to a different DSP amongst the 7.

3.2 Implemented Classical PI/PD Controllers

At the lowest level, all control modes close the loop around the error between the desired actuator torque and the sensed torque. In each case, the inner torque control loop regulates the current passing through the Maxon RE16 DC minimotor at a sample time $T_s = 100\mu$s. Pure force control uses a Proportional Integrator controller whose gains are tuned to limit overshoots and static error.

In the beginning of this project there were two possible control types: position and torque control. One of the objectives of this work, as presented in section 1.3, was to substitute the classical proportional-derivative position controllers which have been tuned manually by robust controllers using modern control theory to achieve better performances for dexterous manipulation. However, the structure of the torque control has not been modified during the project because it presented satisfactory performances for the PWM signal generations. Figure 3.3 shows the 3 nested loops (position, velocity and current) structure used to drive the motors.

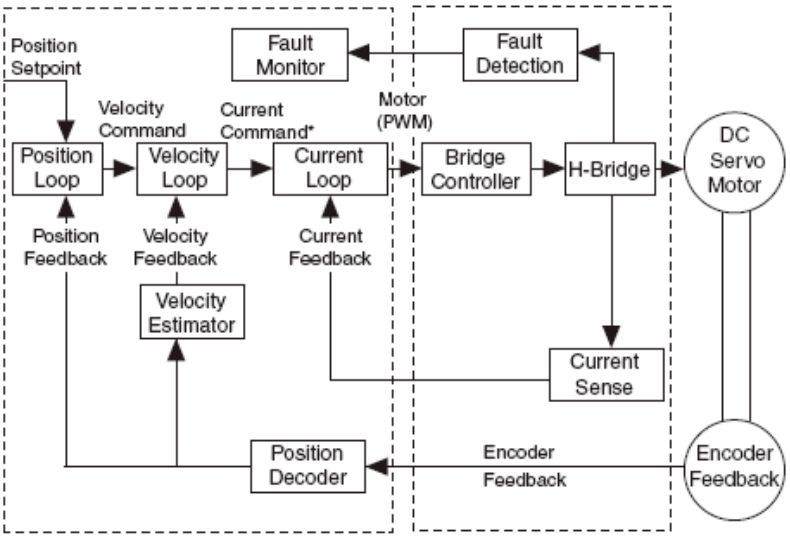

Figure 3.3: General motion controller structure using 3 nested loops [21]

Despite having these 3 loops, it was normally more interesting to give position and current set-points, thus the velocity loop can be viewed as a derivative term for the position loop. In addition to this previous figure, a module of trajectory generation was implemented on the DSPs so that a smooth (S-curves) trajectory could be performed when the unit was controlled in position.

The internal loop of torque control is always present in the final controller structure. For the robust controllers developed in chapter 7 they are neglected because the torque control loop is much faster than the position one and then we can consider that the torque reference given appears directly on the output (in that case the output is the open-loop system's input). In Figure 3.4 one can see grasps of various types of objects using the different types of control modes, either position or torque (current).

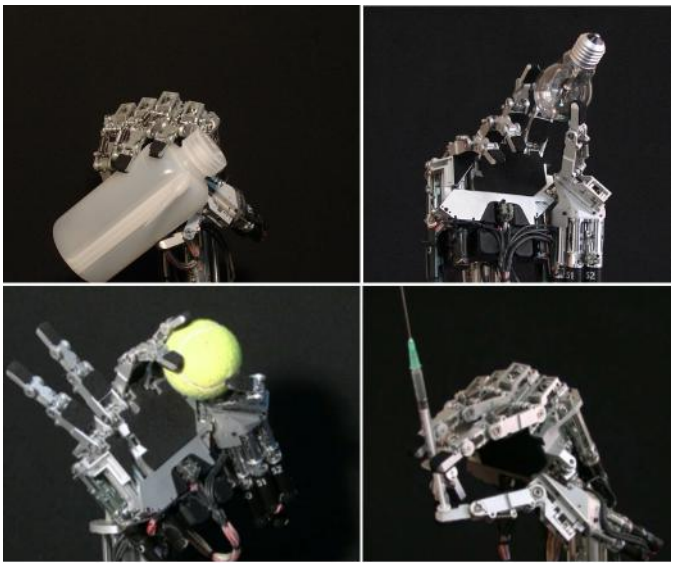

Figure 3.4: Grasps of various objects using the CEA dexterous hand

3.3 Interfacing High and Low Level Control

In order to simplify and make the tests faster to implement, a Matlab/Simulink interface (using a library that forces real time into the simulation) was created to manipulate each DoF of the hand. Even though, the system is totally compatible and prepared for a ROS interface which would be way preferable for more complex applications such as the implementation of high-level control algorithms for in-hand manipulation.

Figure 3.5 shows the interface created to send the set-points to the controllers. It allows us to easily send complex references at the articular level. The maximum rate of information acquisition/sending with this interface, within the UDP protocol, is $100Hz$, which is satisfactory for the tests we performed.

Once again, this is a simple interface that acts like a basic supervisory controller, and it cannot offer real-time applications. In order to do so, an alternative

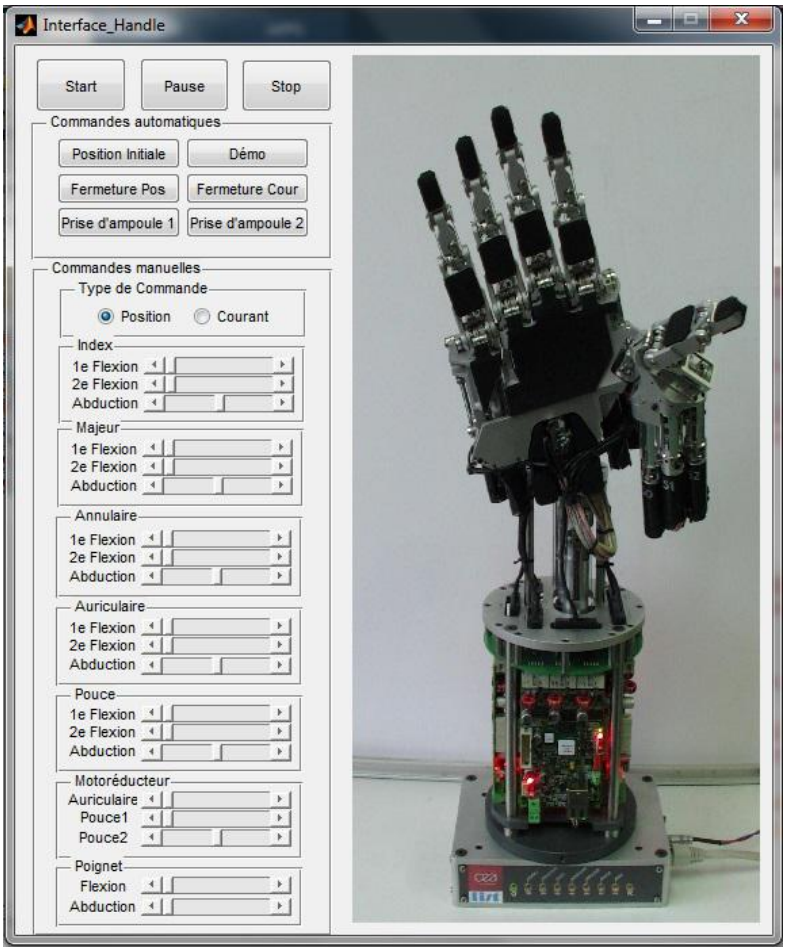

Figure 3.5: Matlab/Simulink interface between the host-PC and the axes' controllers

using ROS [3] and Xenomai [4] (or other RTOS [5]) within a real-time communication bus would be much more appropriate.

For the purpose of the work developed on this project, however, this friendly interface has shown itself practical and sufficient for the tests we performed. The only exception was when faster acquisition was required to plot some results, but, in that case, we stored these points on a vector inside the DSP's memory and send then to the host-PC whenever it was possible.

The second part of this report starts on the next chapter and the concepts presented so far, hopefully, will be useful for a better comprehension of the subject. Part II begins with torque experiments in order to build an algorithm of contact force estimation between fingers and objects and is followed by position experiments which will lead to the development of robust decentralized position controllers.

3. Robot Operating System
4. Real-time kernel for Linux
5. Real-Time Operating System

Part II

Force Estimation and Robust Control

Chapter 4

Torque Experiments

This chapter is devoted to the performed torque experiments which were necessary to explore self-sensing principle, that provides a highly integrated method for sensing the force applied by the hand to an object at the contact point. First, the force estimation algorithm and its main idea is explored and then validation tests are carried out until the end of the chapter. For the sake of a better understanding, let a wrench F be defined as a 6×1 generalized force, which is composed by a pure 3×1 force f and a pure 3×1 collinear moment τ.

4.1 Force Sensing Strategy considerations

The configuration-dependent body manipulator Jacobian matrix $J_{st}^{b}(q)$ of a 3 Axes Unit relates wrench $F_t = \begin{bmatrix} f_t & \tau_t \end{bmatrix}^{\mathsf{T}}$ applied at the origin of a given frame and the resulting joint torques τ_F [20]:

$$F_t = J_{st}^{b}(q)^{-\mathsf{T}} \tau_F \tag{4.1}$$

where $A^{-\mathsf{T}}$ denotes the inverse of the transpose (or equally transpose of the inverse) of the matrix A. Such relationship implies that a 3×1 torque vector is needed to compute the 3×1 pure contact force vector f_t, which is the first element of the wrench F_t. Note the Jacobian matrix calculated for any point between axes 2 and 3 will only take into account the effect of torques τ_1 and τ_2. Thus, for contact points between axes 2 and 3, no force can be estimated in the direction of the common perpendicular to axes 1 and 2 based on (4.1): only 2D forces can be measured. For any contact point located downstream axis 3, as it is often the case for tightening forces in dexterous manipulation tasks, the proprioceptive sensing permits 3D force estimation as we can use the information coming from torques measured in axes 1, 2 and 3 (Fig. 4.1).

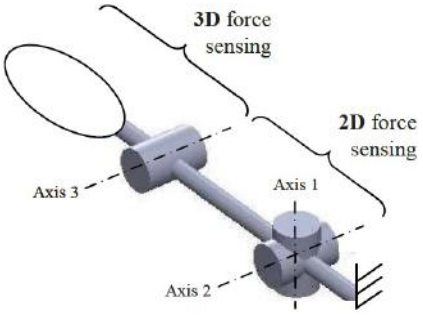

Figure 4.1: Proprioceptive sensing capabilities with the 3 Axes Unit

Contact force estimate

Force applied by a contact is modeled as a wrench F_c applied at the origin of the frame C located at the contact point between finger and the manipulated object, and attached to the phalanx where the contact occurs. Fig. 4.2 illustrates this for the case of a contact point located in the last phalanx, where the end-effector frame B is associated to the phalanx where the contact takes place. Mapping from frame C to frame B is given by g_{bc}, built from the rotation matrix $\mathbf{R}$ and the contact point coordinates with respect to the end-effector frame $p_{bc} = \left[x_c^b, y_c^b, z_c^b\right]^T$. The rotation matrix (Fig. 4.2) $\mathbf{R} = R_{bc}$ represents the pure rotation of $q_4 = c\,q_3$ around x axis because it rotates Frame B (last phalanx) onto Frame C (contact point). If the origin frame was not the last phalanx, but another one closer to the base, it would only be necessary to utilize the homogeneous transformation matrices computed with the Denavit-Hartenberg (DH) parameters, used to obtain the geometric model of the robot and then its natural Jacobian as detailed in [15, 16].

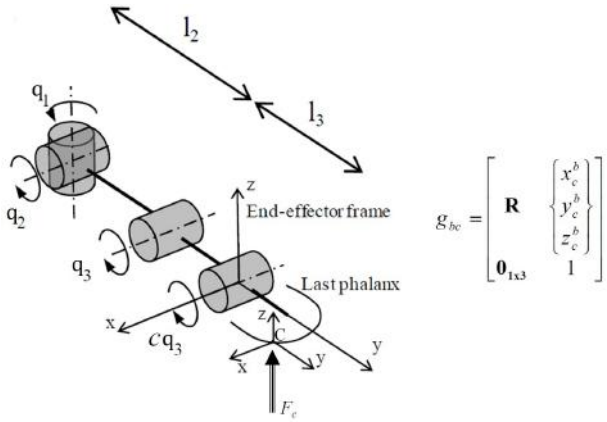

Figure 4.2: Kinematics of the 3 axes unit with contact force representation (g_{bc} denotes the forward kinematics transformation from the contact frame to the end-effector frame attached to the last phalanx).

A wrench applied at the origin of the contact frame is mapped to a wrench

applied at the end-effector frame by the following expression [20]:

$$F_b = Ad_{g_{bc}}^{-\mathsf{T}} F_c \tag{4.2}$$

in which $Ad_{g_{bc}}$ is a 6×6 matrix representing the adjoint transformation associated with the homogeneous transformation g_{bc}. It can be computed as follows:

$$Ad_{g_{bc}}^{-\mathsf{T}} = \begin{bmatrix} R_{bc}^{\mathsf{T}} & -R_{bc}^{\mathsf{T}}\, \hat{p_{bc}} \\ 0 & R_{bc}^{\mathsf{T}} \end{bmatrix} \tag{4.3}$$

For the case of contact point in the last phalanx, the joint torques that produce a desired contact wrench applied to the object are given by

$$\tau_F\left(q\right) = J_{st}^{b}\left(q\right)^{\mathsf{T}} Ad_{g_{bc}}^{-\mathsf{T}} F_c \tag{4.4}$$

In quasi-static operating modes, the finger dynamics in contact with a manipulated object simplifies into

$$\tau_F(q) = N(q, \dot{q}) - \tau(q) \tag{4.5}$$

where $N(q, \dot{q})$ takes into account gravity $G(q)$ and friction $\tau_f(\dot{q})$ terms. The wrench F_c applied at the origin of the contact frame C can be deduced combining equations 2.9 (rewritten bellow), 4.4 and 4.5. The influence of the external forces F_c applied at the fingertip are then sensed through the overall measured current passing through the shunt resistor of each DC motors and the joint angles variation q, which are measured.

$$\tau\left(q\right) = Pf - P_s K \Delta h_s q$$

4.2 Experimental Estimation

This section is devoted to the experimental validation of our proposed force sensing strategy.

Experimental test bench

To evaluate the contact force estimate, an external force sensor (Futek LSB200) has been used to have a reference measure of the contact force produced by the 3-axes unit fingertip. In addition, in order to measure directly the joint angles extra position sensors have been temporarily mounted on the 3-axes unit. These sensors are MCP05 potentiometers from MegaTron$^{\text{TM}}$that have been

used for absolute measurement of each joint shaft. The analog output signals from the calibrated sensors have been connected to a standalone 16-bit analog digital converter card, which corresponds to a resolution of about 0.005 degrees per axis.

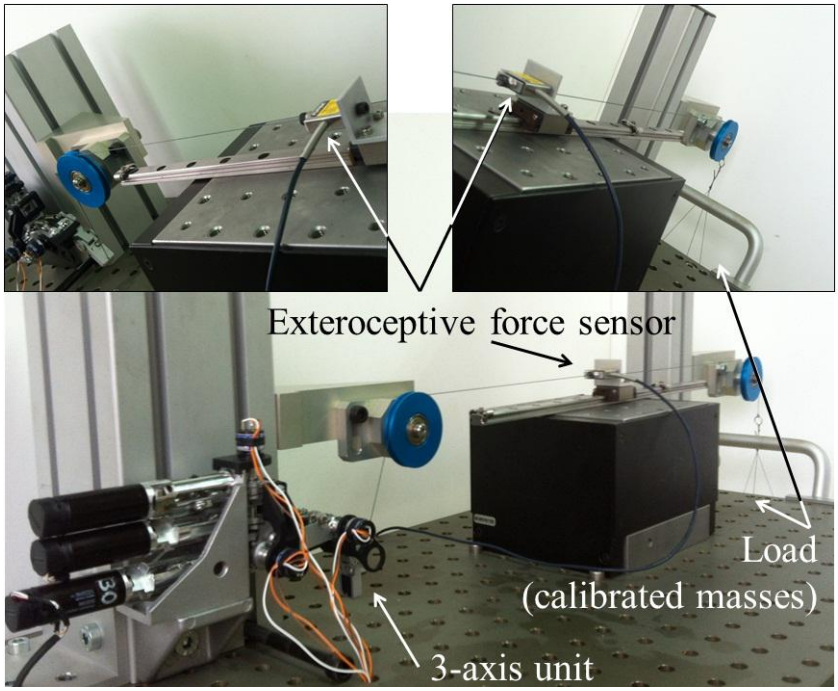

Figure 4.3: Experimental test bench for applying contact force using exteroceptive force sensor (Futek LSB200) measurement and calibrated loads.

In the following, we suppose that the adjoint transformation associated with g_{bc} is presumed a priori known. In a practical way, that means that the contact point C should be estimated on-line thanks to an appropriate contact/pressure sensor technology. Let us note that only information about the contact point location is needed here, requiring good spatial resolution even with low-resolution sensors; from this information our proposed approach is able to achieve quantitative force estimation. As tactile sensing technology is not the scope of the present paper, the exact coordinates $\left[x_c^b, y_c^b, z_c^b\right]^T$ of the contact point at the end of the intermediate phalanx are recorded beforehand. When the cable is pulled by the torque controlled fingertip over the pulley block, a counterforce is created at the contact point C due to external loads (Fig. 4.3). Different loads can be achieved thanks to calibrated masses m. The exteroceptive force sensor mounted along the cable records the exact amount of force applied at the fingertip.

In the following, experiments have been carried out on a 3 Axes Unit, in which the abduction/adduction and first flexion movements have been blocked. Only current and position relative to the motor that controls the mechanically coupled flexions of intermediate q_3 and intermediate cq_3 phalanges are taken into account.

Let us note that such configuration is by far the most complex one from a practical point of view, since it corresponds to a configuration with coupled movements and with the shortest moment arm, resulting in the worst force sensitivity at the joint level. According to (4.4), the theoretical joint torque at the third axis is depending on the force components along y and z axes as follows:

$$\tau_{F_3} = f_c^z l_3 cos\left(cq_3\right) - f_c^y l_3 sin\left(cq_3\right) + (c+1)\left(f_c^z y_c^b - f_c^y z_c^b\right) \tag{4.6}$$

where $[f_c^x, f_c^y, f_c^z, 0, 0, 0]^\mathsf{T}$. f_c^x is zero because no force is applied along this direction.

Contact force considerations

Equation (4.6) shows there is always a possible combination of F_c^y and F_c^z for which $\tau_{F_3} = 0$. This combination of F_c^y and F_c^z gives a direction s in the y, z plane along which an arbitrary force applied to the finger can be counterbalanced with $\tau_{F_3} = 0$. In other words, forces acting along this direction s are not observable from the actuator side and therefore they cannot be estimated by the self-sensing ability. Thus, using only the measured value of τ_{F_3}, we can only estimate the projection of the contact forces onto a direction $s^\perp$ which is perpendicular to s. Those directions physically represent the axes z ($s^\perp$) and y (s) of the medial phalanx frame (second flexion/extension) since one only motor is not capable of sensing forces applied on its y direction because it does not prevent the axis movement, the force sensed is always perpendicular to rotational displacement, which is z. A simple scheme, considering only the motor frame, is shown in Figure 4.4.

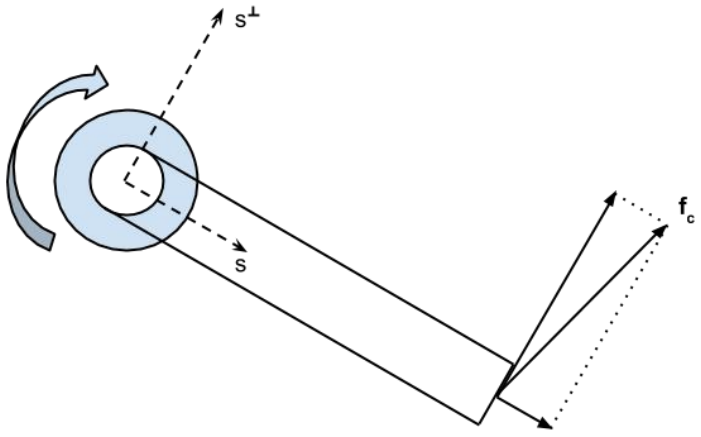

Figure 4.4: Scheme to identify s and $s^\perp$ directions

The cable has been conveniently arranged during the experiments to be aligned with $s^\perp$. Note that when using the measured values of $\tau_{F_1}, \tau_{F_2}, \tau_{F_3}$, we will be able to estimate the three components of any arbitrary 3D contact force.

When executing dexterous manipulation tasks or grasping objects with robotic hand, contact force at the fingertips has to remain positive toward the object surface and its direction has to be within the friction force limits shown as a friction cone. The friction constraint for a point contact is assumed to conform to Coulomb's law:

$$\sqrt{(F_c^x)^2 + (F_c^y)^2} \leq \mu F_c^z \text{ and } F_c^z > 0 \tag{4.7}$$

where μ defines friction coefficient at contact point C. In practice, such constraint implies that F_c^z is much more significant than F_c^y. Therefore, according to (4.6), it can be verified that τ_{F_3} remains always positive under friction constraints during experiments.

Friction torque modeling

An accurate estimation of the dry friction torque is required for the procedure of the force estimation especially for low velocities and/or for external load variations due to force contact. According to [22, 23], an extended friction model to capture load effect in finger joint has been investigated. Viscous friction phenomenon will not be considered in our case, since dry friction torque has been experimentally evaluated as much more significant than viscous friction torque at low speed. As the inertial load and gravity torque due to the lightweight phalanges of each finger, as well as spring effect, are much less significant than the external force load τ_F applied at the fingertip, the torque load τ_{load} at the joint level is assumed to be mainly due to the contact force load τ_F. The effect of τ_{F_3} is analyzed by means of experiments on the 3 Axes Unit in the following. Justified by its significance, load torque will then be included in an extended static friction model.

As per [22], the dry friction load dependency provokes a shifting on the usual Coulomb Force F_C threshold present on the friction curve as depicted in figure 4.5.

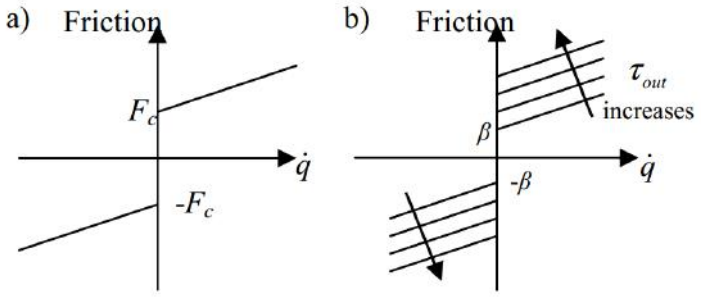

Figure 4.5: (a) Usual friction model with constant F_C. (b) Parametric effect of the load on friction model. [22]

Following the theoretical analysis exposed in [23], two behaviors of the back-

drivable actuation unit have to be distinguished according to the sign of the output power $P_{out} = \tau_F \dot{q}$. Each case, $P_{out} > 0$ or $P_{out} < 0$, defines a specific dry friction model, depending if the threshold torque corresponds to the minimum effort to move the actuator either from the motor side or the load side. Having previously noticed that $\tau_{F_3} > 0$, the sign of P_{out} is only defined with the sign of $\dot{q}$. This behavior is shown in more details in [22], but figure 4.6 gives a general idea.

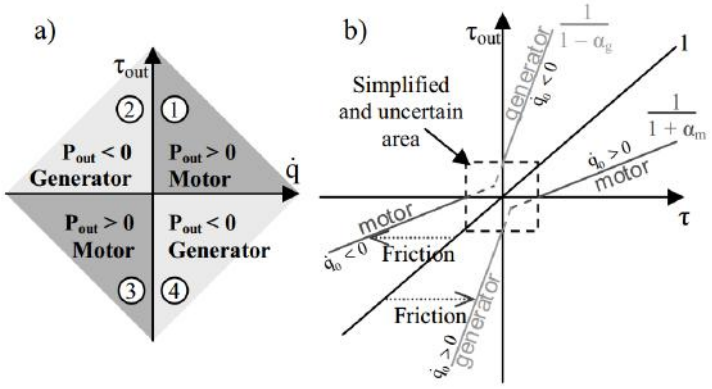

Figure 4.6: (a) Four quadrants frame ($\dot{q}$, τ_{out}) for motor/generator behavior. (b) Asymmetrical friction for velocity $\dot{q}_0$ and definition of the uncertain area. [22]

While the finger joint is actuated by motor in the positive sense of q for bending movement downwards, the case where $\dot{q} < 0$ corresponds to the configuration where the finger is moving back in extension due to the application of external load, i.e. the backdrivable actuation sense in our case. For that particular case, the dry friction torque τ_f is described as being dependent on external load. On the contrary, for the case where $\dot{q} > 0$, i.e. the finger is actually bending movement downwards in flexion under the motor torque only, the dry friction torque is only defined by the direct torque threshold $\tau_{f0_{\dot{q}>0}}$. Finally, the load-velocity friction model is expressed as follows:

$$\tau_f = \begin{cases} -\tau_{f0_{\dot{q}<0}} - A\tau_{load} & \text{if } \dot{q} < 0, \\ \tau_{f0_{\dot{q}>0}} & \text{if } \dot{q} > 0 \end{cases} \tag{4.8}$$

where A is a real constant quantity to be identified experimentally for each axis. Experiments were carried out to characterize the load-dependent friction model for the third axis q_3 when applying calibrated masses at the fingertip. The dry friction torque is deduced from the overall motor torque when subtracting spring and gravity torques contributions. Experimental data shows the linear dependence of dry friction torque with respect to τ_{load} and permits to identify the friction model for $\dot{q} < 0$ (Fig. 4.7).

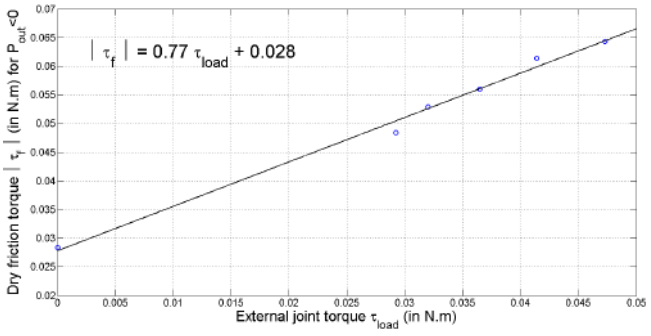

Figure 4.7: Identified dry friction torque dependence for the third axis q_3 according to calibrated external loads $\tau_{load} \cong \tau_{F_3}$ for different masses m applied at the fingertip (A=0.77 and $\tau_{f0_{\dot{q}<0}} = 0.028$ N.m).

Experimental contact force observation

In virtue of backdrivability, interaction between fingers' hand and contact force induces torque perturbations at motors level. When controlled in torque mode, motors ensure reference torque values at the output, resulting in a certain amount of finger displacement determined by the object being grasped. The amount $\|F_c\|$ of external force applied at the fingertip is then estimated from relationships (4.4), (4.5) and (4.8).

For the experimental protocols previously described, only the two intermediate joints are free to move; the remaining joints have been blocked by mechanical stops added for the experiment. This way, only one motor is used for the purpose of contact force estimate, which is controlled in torque. When the motor is given a step torque reference, the joint undergoes a certain displacement and contact forces are measured. Different contact forces are obtained through different values of the calibrated masses. Such strategy permits to efficiently capture and estimate contact force applied at the 3-axes unit fingertip for different external loads ($0.6N$, $0.9N$ and $1.0N$ on Fig. 4.8).

At the beginning, a step reference is given to the torque controller. Then, a certain amount of mass is added to the counterweight and is finally removed at a certain time, both manipulations in quasi-static conditions. Upper Fig. 4.8 shows the motor current following the step reference throughout the whole experiment, lower Fig. 4.8 shows a certain displacement of the measured joint angle, and middle Fig. 4.8 superposes the measured and the estimated contact forces, caused by the external loads. The lowest contact force detected was about 0.4N, which indicates the contact force sensitivity threshold of the measuring strategy. This is a promising result that validates our sensing approach and its potential complementarity with tactile skin sensing solutions.

From now on, positions experiments for dynamic characterization and its consequences will be the main subject of this report. Next chapter shows important

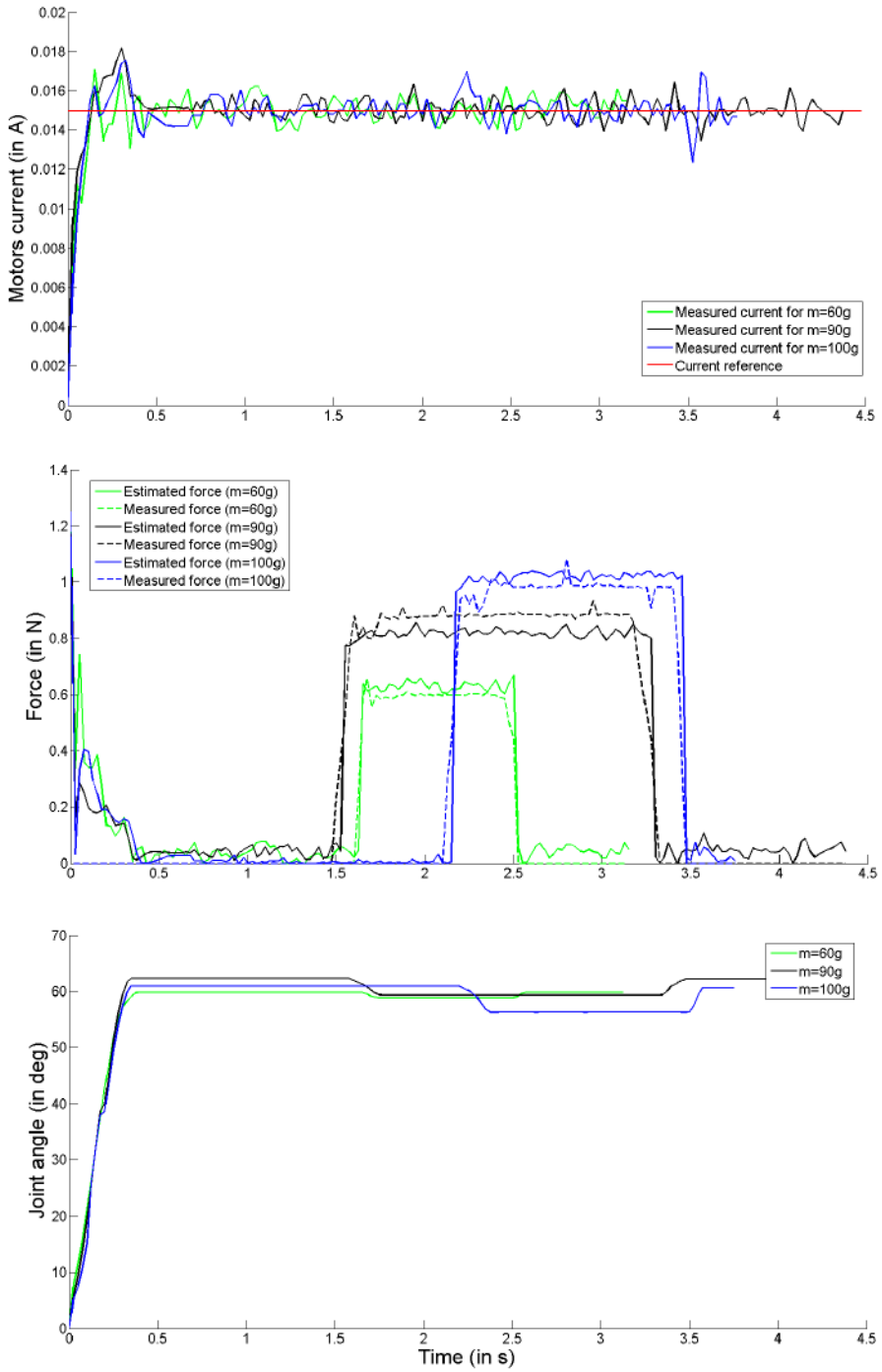

Figure 4.8: Experimental contact force estimation based on proprioceptive measurement on flexion axis q_3 (q_1 and q_2 are kept constant) and comparison with an exteroceptive force sensor measurement for different external loads

properties that will be used for the robust decentralized poistion controller in chapters 6 and 7.

Chapter 5

Position Experiments

This chapter is devoted to the controller synthesis key elements, that will be exploited on the following chapters. It starts by establishing the relationship between motor and joint angles and showing how the control oriented design of the hand has minimized the coupling between axes, favoring a decentralized control strategy. Also, some non-linear phenomena are outlined so that the design guidelines can be established.

5.1 From Motor to Joint Frame

Kinematic relationship between motors $\theta = [\theta_1, \theta_2, \theta_3]^\mathsf{T}$ and joints $q = [q_1, q_2, q_3]^\mathsf{T}$ motions is given by 2.13 and in quasi-static movements the relation can be written as :

$$\theta = T\, q \qquad \Leftrightarrow \qquad q = T^{-1}\, \theta$$

where,

$$T = \begin{pmatrix} \frac{-r_1}{R_{11}} & 0 & 0 \\ 0 & \frac{-r_2}{R_{22}} & 0 \\ 0 & \frac{-r_{3a}}{R_{33}} & \frac{-r_{3b}}{R_{33}} \end{pmatrix} \Rightarrow T^{-1} = \begin{pmatrix} \frac{-R_{11}}{r_1} & 0 & 0 \\ 0 & \frac{-R_{22}}{r_2} & 0 \\ 0 & \frac{R_{22}\, r_{3a}}{r_2\, r_{3b}} & \frac{-R_{33}}{r_{3b}} \end{pmatrix} \tag{5.1}$$

where $R_{ii} = -\frac{p_i}{4\pi}$ are the elements of the diagonal matrix R which relates the motor angles θ with linear displacements h generated by the ball-screw mechanism.

One may note there is only one *off-diagonal* element in equation 5.1 and if we take a look into the expression of T^{-1} it has an opposite sign comparing to the other elements since all pulley radius are obviously positive and the R_{ii} negative.

Continuing with T^{-1}, the fact that this matrix is not diagonal means that there is a static coupling in the transmission. In our case, if a set-point is done in motor 2 ($\theta_2 \neq 0$) the second flexion/extension moves on the opposite sense of a factor $\frac{R_{22}\, r_{3a}}{r_2\, r_{3b}}\, \theta_2$.

In the next session the system coupling on the motor-to-joint transmission is presented in practice.

5.2 Mechanical Decoupled Axes

Independent joint control is a desired target since it allows a decoupled analysis of the closed-loop system using single-input/single-output (SISO) classical control schemes. This simplification of the control strategy is relevant in practical implementations, due to the complexity of multiple-input/multiple-output (MIMO) control schemes. In this section, the decoupling of the DoF is experimentally validated through an analysis of independent joint control in the low frequency range. For this purpose we are using simple classic PD controllers for each axis.

Our previously optimized tendon routing results in a motor-to-joint transformation matrix T^{-1} which theoretically exhibits the same quasi-diagonal structure as the coupling matrix P. In a practical way, extra position sensors have been once again, as per the torque experiments, temporarily mounted on each joint θ_i of the 3 Axes Unit (Fig. 5.1).

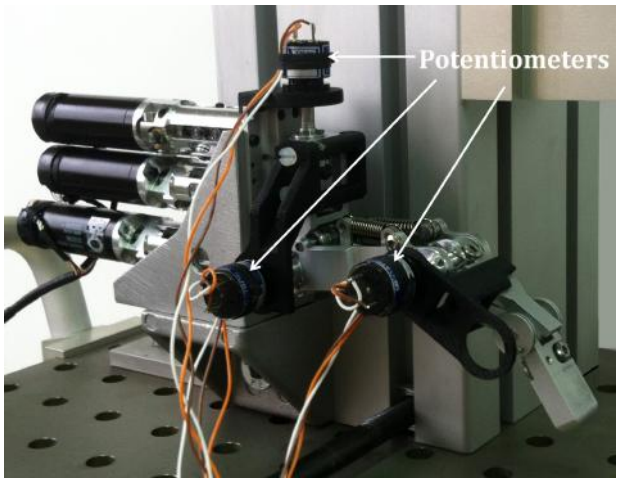

Figure 5.1: Test bench to evaluate couplings and performances of the motor-to-joint transmissions.

For each experiment, one targeted motor is controlled in position while the other two motors are left free to move.

– Firstly, the maximum cross couplings in quasi-static operations between abduction/adduction motions (around axis 1) and both proximal and intermediate flexion/extension motions (around axes 2 and 3) are below −39 dB (Fig. 5.2a). Thus, all components in the first line and first column of the transformation matrix T are indeed null terms in practice.

– Then, the maximum cross couplings between the last flexion/extension motion (around the axis 3) and the other two motions (around axes 2 and 3) are below −28 dB (Fig. 5.2b). In the sub-matrix of T^{-1} related to both first and second flexion/extension motions, the extra-diagonal components are also effectively null terms in practice. Nevertheless, such theoretical coupling will be taken into account for the synthesis of the SISO H_∞ controllers in chapter 7.

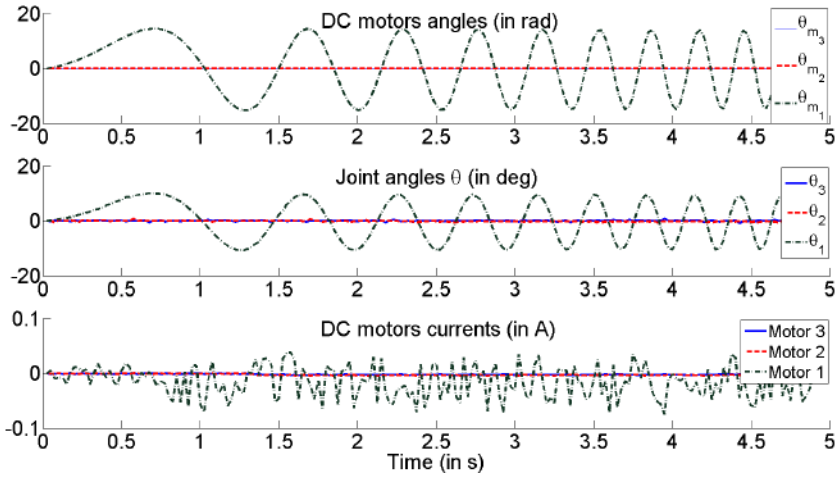

(a) Abduction/adduction motion decoupling

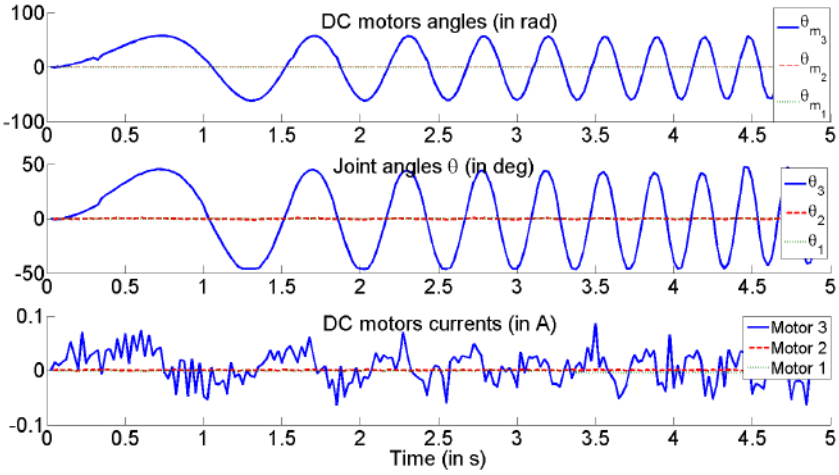

(b) Last flexion/extension motion decoupling

Figure 5.2: Motion decoupling in quasi-static operation

These two open-loop experimental characterizations imply that our theoretical tendon arrangement is efficient in reducing the influence of the residual kinematic coupling effects. Even the influence of the off-diagonal term in T^{-1} is considerably low so that SISO controller could be performed. Nevertheless, another measure of axes coupling (RGA [1]) will be introduced on the next chapter because it considers the coupling over all frequency spectrum, which will be essential on

1. Relative Gain Array

our frequency-domain approach for controller synthesis.

5.3 Non-linearity and compliance phenomena

Dynamics of the transmission system can be influenced by non-linearity (such as friction) and compliance phenomena, which often lead to undesired hysteresis and discontinuity behaviors [24]. Any of these can reduce the performance of the system: hysteresis implies difference in the transmission output when it is reached from two opposite directions, while discontinuity induces a lost motion after reversing direction as for backlash phenomenon.

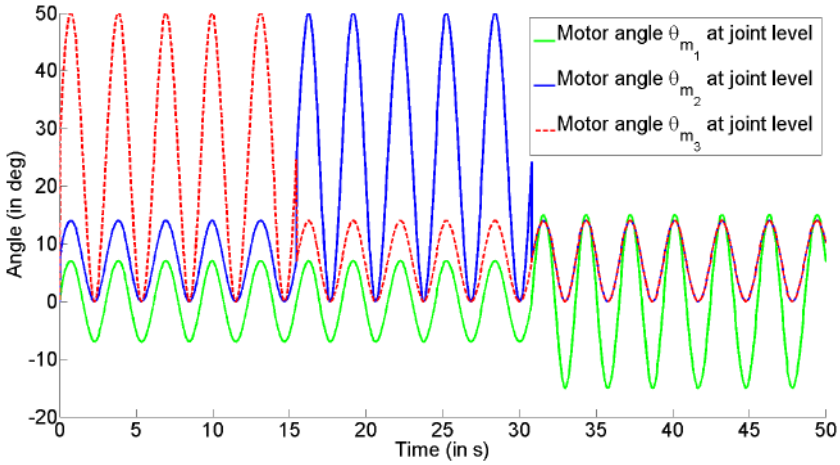

Figure 5.3: Simultaneous sine trajectories for motor angles represented at the joint level through the theoretical static transformation matrix T^{-1}.

To analyze them, simultaneous quasi-static sinusoidal trajectories have been applied as inputs for each motor of the 3 Axes Unit (Fig. 5.3). Let note that considering simultaneous trajectories permits to evaluate the performances in precision for the worst-case analysis (considering the fully actuated transmission system). Two constant amplitudes have been considered for each axis. These amplitudes correspond to both small and large ranges of motion (-7 to 7 deg and -15 to 15 deg for axis 1, 0 to 13 deg and 0 to 50 deg for axes 2 and 3), while the frequency is kept to 0.3Hz to consider quasi-static dry friction phenomenon.

The measured motor position θ_i is plotted as a function of the measured joint position q_i (Fig. 5.4a for abduction/adduction motion, Fig. 5.4b and Fig. 5.4c for both flexion motions). For each axis, two stable loops have been experimentally obtained (one per motion amplitude), and a maximum relative error of 8% in the cable-driven transmission system has been identified. In our case, these effects can reasonably be assumed small compared to other robot hands using tendon-based transmission mechanism [25] [26] [27].

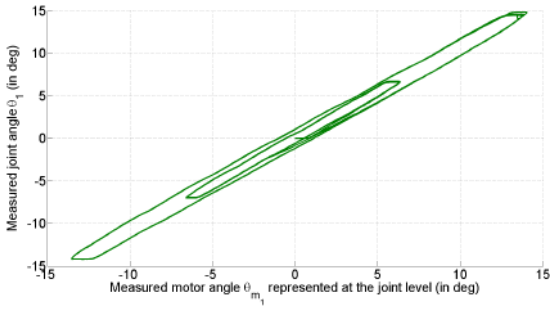

(a) Deadband-shaped loop for the first axis

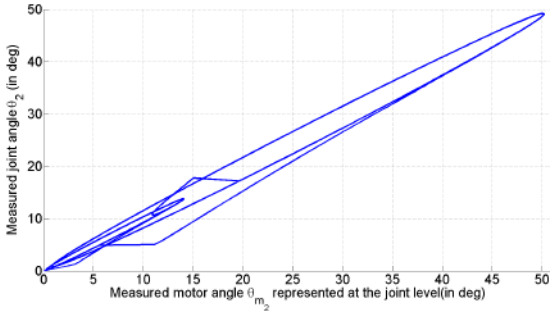

(b) Hysteresis loops for the second joint

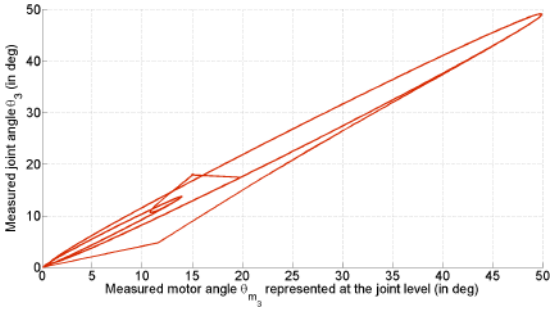

(c) Hysteresis loops for the third axis

Figure 5.4: Deadband and Hysteresis loops of the behavior between joint and motor angles (represented at the joint level)

The input-output cycles exhibited on Fig. 5.4a, Fig. 5.4b and Fig. 5.4c have distinct shapes according to the considered axis:

– ellipsoid-shaped hysteresis for both flexion motions of the finger unit (Fig. 5.4b and Fig. 5.4c); it can be attributed to compliance phenomena [28]. Areas of such rate-dependent hysteresis loops are representative of the energetic and power losses due to the viscoelasticity behavior of the cables. From a mechanical point of view, it should be recalled that the degrees of freedom related to both flexion motions are driven using cables routing with antagonistic springs. Consequently, it induces lag between fingertips and actuation units, because of viscoelasticity behavior of the tendons [29] [30]. Lags are less than 47 ms for axis 2 (Fig. 5.4b) and 50 ms for axis 3 (Fig. 5.4c), partly because of the optimized cable arrangement and the shortened length of tendons (a few centimeters maximum).

– deadband-shaped loop behavior for abduction/adduction motion (Fig. 5.4a). It distinguishes from previous ellipsoid-shaped hysteresis loops by the distinct discontinuities exhibited at both extremes. In our configuration, transmission system related to abduction/adduction motion is based on a very short closed-loop routing of cables. As the cable length is drastically reduced for the first axis (Fig. 2.3), the effect

of cable compliance is almost nonexistent (no ellipsoid-shaped hysteresis). However, the preload effects, which are required for the assembly of that specific closed-loop routing of cables, associated to mechanical play in the motor-to-joint transmission, are a bit more significant in that case. This rate-independent behavior results in small non-uniform joint motions with variable deadband loops.

5.4 Design guidelines

From the deduced equations 2.15 and 2.16 (rewritten bellow) and from the results previously presented on this chapter, the design guidelines regarding dynamics in motor-to-joint transmission can be summarized as follows:

$$\widetilde{M}(q)\,\ddot{q} + \widetilde{C}(q,\dot{q})\,\dot{q} + \widetilde{K}\,q + N(q) = T^{\mathsf{T}} K_{em}\, i_m$$

where,

$$\begin{aligned} \widetilde{M}(q) &= M(q) + T^{\mathsf{T}} J_m T \\ \widetilde{C}(q,\dot{q}) &= C(q,\dot{q}) + T^{\mathsf{T}} B_m T \\ \widetilde{K} &= P_s K \Delta h_s \end{aligned}$$

i In our case of quasi-diagonal coupling matrix T associated with small reduction ratio n_i, equation (2.16) reveals that the serial finger dynamics are approximately given by decoupled second-order equations. In addition, it leads to almost constant coefficients represented by motor-side inertia and viscous friction phenomena. The resulting system to be controlled can be seen as an almost decoupled linear time-invariant system. This feature avoids the necessity of a full multivariable controller or even SISO controllers with hard constraints on disturbances rejection.

ii In the same perspective, considering placement of actuators in the palm/forearm instead of integrating directly them in the phalanxes, tends to decrease the influence of inertia due to the moving links $M(q)$ relatively to the reflected motor inertia ($T^{\mathsf{T}} J_m T$).

iii As the mass of each phalanx link is decreased by the same way, influence of disturbance gravitational and Coriolis/Centrifuge terms are also not so predominant.

iv Reducing the influence of inertial loads $M(q)$ also tends to minimize the frequency variation of the flexible modes due to spring effects at motor-side [31]. In that sense, configurations for which actuators are located outside of the phalanges are preferred here from a control perspective.

v Joint stiffness torques due to return springs $\tilde{K}$ into the proposed single-acting actuation principle is also almost decoupled between all the axes of the 3 axes unit due to the quasi-diagonal structure of matrix P_s.

At the end, taking all these considerations into account for the hand design, very few dispersion into all frequency spectrum of the nonlinear system (2.15) are noticed. Thus, the techniques employed to the controller synthesis, which will be presented on the following chapters, are reasonably justified.

Chapter 6

Model formulation for controller design

The previous statements and the conclusions drawn so far, lead to a frequency-domain approach for the controller design of the 3-axes unit. Its dynamics given by the nonlinear differential equation (2.15) can be reasonably linearized around a chosen nominal point $\left(q_0 = \begin{bmatrix} 0 & \frac{\pi}{4} & \frac{\pi}{4} \end{bmatrix}^{\mathsf{T}}$ and $\dot{q}_0 = \begin{bmatrix} \frac{\pi}{4} & \frac{\pi}{4} & \frac{\pi}{4} \end{bmatrix}^{\mathsf{T}}\right)$ in order to be locally rewritten as a Linear Time Invariant (LTI) system. The model has been reformulated to a robust control design perspective. Moreover, from the announced design guidelines, low time-varying coefficients of $M(q)$ inertia matrix, as well as nonlinear terms of $C(\theta, \dot{\theta})$, can be treated as uncertainties around that locally LTI system.

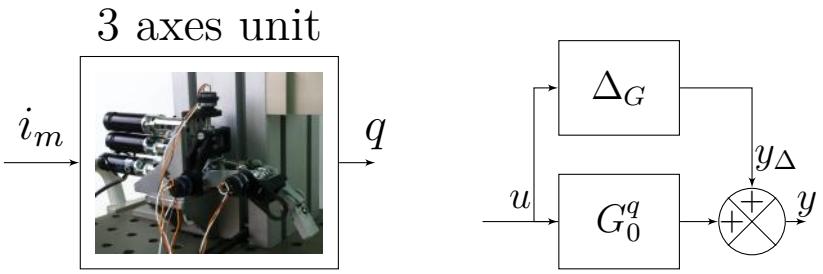

Figure 6.1: 3 axes unit system and equivalent uncertain system

For instance, the variations between its local representation and the complete nonlinear system are described by an additive uncertainty Δ_G around a nominal configuration as depicted in (Fig. 6.1). The local transfer matrix form $G_0^q(s) \in \mathbb{C}^{3\times3}$ around the nominal point is introduced as follows:

$$Q(s) = G_0^q(s) I_m(s) \tag{6.1}$$

where s designates *Laplace* operator. Robust stability of the whole system with Δ_G is named 1^{st} *condition* and will be guarantied using Small Gain Theorem [32] in the section relative to the controller tuning since this condition must, obviously, be respected by the controller.

The reader may note that computed torque control could also be applied to simplify the problem in a first instance, generating a pure double integrator system. However the objective of using directly robust control techniques upon the non-linear system was to prove that it was not necessary to feedback linearize the system in order to control it, it is only necessary to treat non-linearities and time-varying terms as additive uncertainties.

6.1 Robust Control

Even if the results treated so far were focused on the joint-side, on this work, articular control is performed driving the DC minimotors for each finger. For instance, the motor shaft position is measured by an encoder and the position control loop is closed considering the coupling matrix T. Hence, as the nominal (design base) system is linear, it does not matter if the motor-to-joint transformation is made upstream (before the controller) or downstream (after the controller), the result is the same and the study of interaction between axes should be performed on joint-side. Thus, for practical reasons, instead of using $G_0^q(s)$, the motor-side transfer-matrix will be considered.

$$G_0^\theta(s) = \frac{\Theta(s)}{I(s)} = \begin{pmatrix} g_{11}^\theta & g_{12}^\theta & g_{13}^\theta \\ g_{21}^\theta & g_{22}^\theta & g_{23}^\theta \\ g_{31}^\theta & g_{32}^\theta & g_{33}^\theta \end{pmatrix} \tag{6.2}$$

whose elements were calculated using Robust Control MATLAB Toolbox as follows:

$$g_{11}^\theta = \frac{2.3543 \cdot 10^5}{s(s+19.46)} \qquad g_{12}^\theta = \frac{4856.3}{(s+19.46)(s^2+3.602s+18.12)}$$

$$g_{21}^\theta = \frac{-4856.3}{(s+19.46)(s^2+3.602s+18.12)} \qquad g_{22}^\theta = \frac{2.2495 \cdot 10^5}{(s^2+3.602s+18.12)}$$

$$g_{31}^\theta = \frac{-1787.2}{(s+19.46)(s^2+3.764s+45.52)} \qquad g_{32}^\theta = \frac{-3368.3\ s(s+0.8521)}{(s^2+3.602s+18.12)(s^2+3.764s+45.52)}$$

$$g_{13}^\theta = \frac{1787.2\ (s+7.694)(s-3.894)}{(s+19.46)(s^2+3.602s+18.12)(s^2+3.764s+45.52)}$$

$$g_{23}^\theta = \frac{-3368.3\ (s^2-1.832s+1189)}{(s^2+3.602s+18.12)(s^2+3.764s+45.52)}$$

$$g_{33}^\theta = \frac{2.3787 \cdot 10^5}{(s^2+3.764s+45.52)}$$

Despite the fact that this matrix is theoretically full, it will be presented on the next sections how the predominant diagonal structure of the plant will be considered for the synthesis of SISO controllers for each axis.

6.2 RGA measure for axes coupling analysis

The Relative Gain Array (RGA) is a very powerful tool to provide a measure of interactions [33]. For each pair of input i/output j the ij-th relative gain is calculated considering two extreme cases: all other loops closed with perfect control and all other loops open. The RGA is defined as the corresponding matrix of relative gains. Considering G_0 the square complex matrix that represents system dynamics, its RGA is defined as follows [34]:

$$RGA(G_0) = \Lambda(G_0) \triangleq G_0 \times (G_0^{-1})^{\mathsf{T}} \tag{6.3}$$

where $\times$ represents the *Hadamard* (or *Schur*) product, i.e. the element-by-element matrix multiplication. The ratio λ_{ij} of the ij-th relative gain between the extreme "open-loop" $g_{0_{ij}}$ and "closed-loop" $\hat{g}_{0_{ij}}$ gains is defined as

$$\lambda_{ij} \triangleq \frac{g_{0_{ij}}}{\hat{g}_{0_{ij}}} = [G_0]_{ij} \times \left[G_0^{-1}\right]_{ji} \tag{6.4}$$

where the term $g_{0_{ij}}(s)$ of matrix G_0 represents, in our case, the influence of input motor current i_{m_i} on output joint angle q_j and $\hat{g}_{0_{ij}}$ is the inverse of the ji-th element of G_0^{-1}. Elements with $\lambda_{ij}(s)$ close to 1 is the key objective to be pursued. It means that the transfer function from input u_i to output y_j is unaffected by closing the other loops.

Analysis of the RGA frequency-varying matrix $\Lambda(G_0)$ for the 3 axes unit permits to formulate several remarks related to our optimized design (Fig. 6.2) :

- When regarding RGA elements close to 1 at crossover frequencies, pairing between inputs and outputs is clear and it tends to associate motor torque i with joint angle i.
- It results from our design that motor-to-joint transmission avoids any couplings over the whole frequency spectrum between abduction/adduction $g_{0_{11}}$ and both flexions motions $g_{0_{ij}}$ with $i, j \geq 2$ (as all components of first line and column of T matrix are null).
- After crossover frequencies, $\Lambda(G_0)$ is equivalent to identity matrix. Indeed, from relationship (2.15), the system dynamics in high-frequency can be

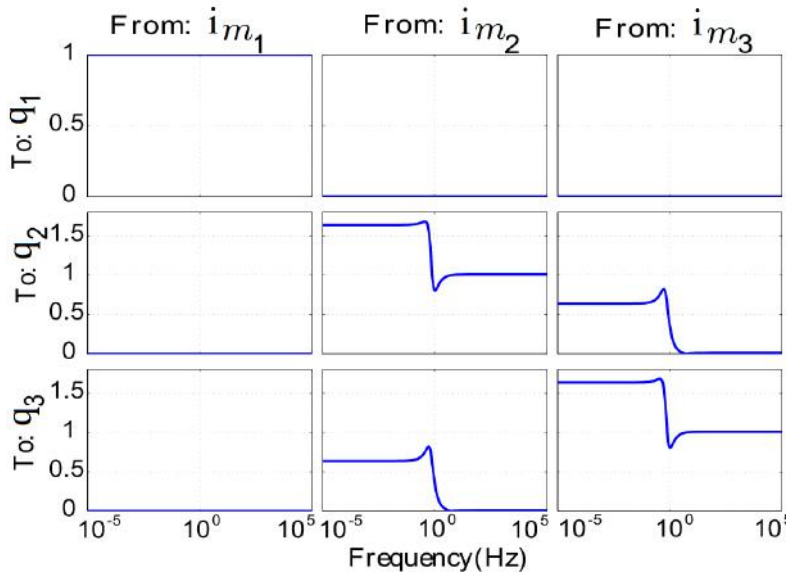

Figure 6.2: Amplitudes of RGA frequency-varying matrix $\Lambda(G_0)$ in absolute values from motor currents i_m to joint angles q.

approximated by:

$$J_m T \ddot{q} = K_{em}\, i_m \tag{6.5}$$

As the transformation matrix T has only one non-null off-diagonal term, it leads to an equivalent high-frequency linear system between motor currents and joint angles, whose transfer matrix $\Lambda(G_0)$ is upper triangular. An important algebraic RGA-property is that the resulting RGA for such triangular system is always the identity matrix [34], proving that the decoupling is valid in high-frequency for all axes of the modular unit, in particular for both flexion motions. Such high-frequency decoupling will ease specifications of disturbances rejection.

– RGA elements for low-frequencies, which are important for control, are small (less than 1.5 in magnitude). It indicates that our design approach, that has brought performances homogeneity among all axes, leads to a plant which is not fundamentally difficult to control due to small interactions and small sensitivity to uncertainty.

6.3 Diagonally dominant plant

Each diagonal element of the controller will be designed based on the corresponding diagonal element $g_{0_{ii}}$ of $G_0(s)$, such that each individual loop is robustly stable and achieves the required performances. In the following, we refer to $\tilde{G}_0 = diag\,(g_{0_{ii}})$ as the matrix consisting of the diagonal elements of $G_0(s)$. To achieve stability of the overall system with all loops closed, interactions must

not cause instability. Property inherent to stability of our optimized mechanical design under decentralized control is exposed below.

With decentralized control, the interactions are given by the off-diagonal elements, that are captured with the $(G_0 - \tilde{G}_0)$ transfer. The interactions can be normalized with respect to diagonal elements of the system transfer matrix as follows:

$$E \triangleq \left(G_0 - \tilde{G}_0\right) \tilde{G}_0^{-1} \tag{6.6}$$

Matrix E can be seen as an additional output multiplicative uncertainty for the nominal diagonal system $\tilde{G}_0$, so that $G_0 = (I + E)\,\tilde{G}_0$. The magnitude of the matrix E is commonly used as an *interaction measure*. According to [34], $\mu(E)$ is the best (least conservative) measure, where $\mu(\cdot)$ designates the structured singular value operator. Thus, the system G_0 is said to be *generalized diagonally dominant* if

$$\mu(E) < 1 \tag{6.7}$$

In our case, the μ-interaction for our optimized 3 Axes Unit system is $\mu(E) = 0.78$. Thus, the plant to be controlled can be very reasonably considered as diagonal $\tilde{G}_0$ (Fig. 6.3)

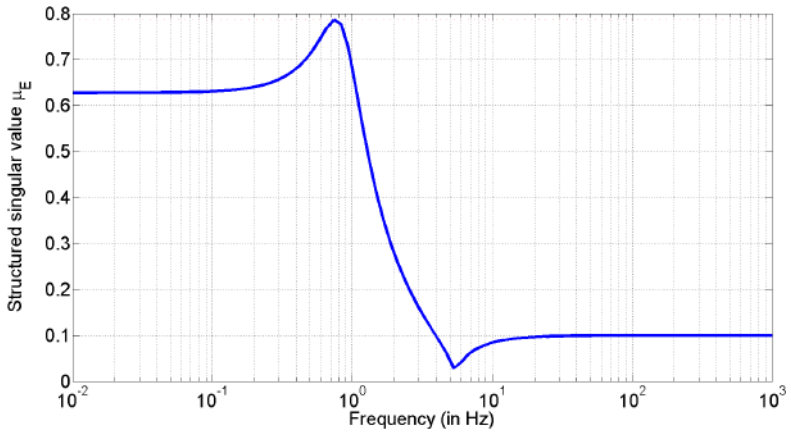

Figure 6.3: Amplitudes of RGA frequency-varying matrix $\Lambda(G_0)$ in absolute values from motor currents i_m to joint angles q.

6.4 Stability analysis of decentralized control

The sensitivity function for the individual loops is defined as

$$\tilde{S} \triangleq \left(I + \tilde{G}_0 K_{fb}\right)^{-1} = diag\left(\frac{1}{1 + \tilde{g}_{0_{ii}} k_{ii}^{fb}}\right) \tag{6.8}$$

Note that $\tilde{S}$ differs from the matrix of diagonal elements of S =

$(I + G_0 K_{fb})^{-1}$. The overall sensitivity function S with all loops closed can be factorized as follows:

$$\underbrace{S}_{\text{overall}} = \underbrace{\tilde{S}}_{\text{individual loops}} \underbrace{\left(I - E\tilde{T}\right)^{-1}}_{\text{interactions}} \tag{6.9}$$

where $\tilde{T} = I - \tilde{S}$ refers to the complementary sensitivity function for the individual loops. According to [35], a sufficient condition for stability of the overall system can be formulated in the least conservative way as follows

$$\left\|\tilde{T}\right\|_\infty < 1/\mu\left(E\right) \tag{6.10}$$

proving that each individual loop is stable by itself. $\|.\|_\infty$ designates the H_∞ norm of a transfer matrix [32]. Thus, stability of the individual loops guarantees internal stability of the overall closed-loop system is provided when individual peaks of $\tilde{T}_i$ are less than $1/\mu\left(E\right) = 1.28$. That condition is named 2^{nd} *condition* and, as the first one, must be respected by decentralized controller to ensure internal stability of the whole system.

Chapter 7 finally presents the development of the H_∞ controllers considering the requirements to be fulfilled by the system in terms of performance and stability.

Chapter 7

Decentralized Control via H_∞ Synthesis

As concluded in section 6.2, a strategy of decentralized control could be employed due to the low level of interaction between axes. Thus, this section is devoted to the synthesis of three robust controllers (one for each axis) for each finger of the CEA multi-dexterous hand.

Considering the fact that time-domain requirements (such as $n\%$ response-time, static error, overshoot, etc) can be easily *translated* on frequency-domain requirements (analog filters) and that the uncertain frequency-domain model representation (section 6.1) has been chosen, the H_∞ synthesis of robust controllers is the one that best fits the project objectives, principally because we focus in high performance requirements for dexterous in-hand manipulation.

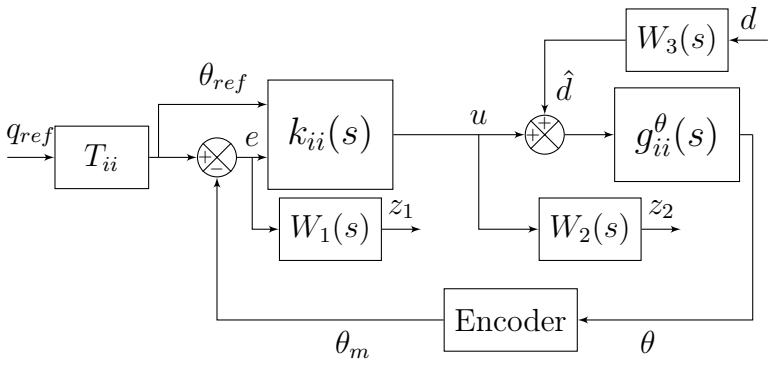

Figure 7.1: Structure of the desired controller with augmented system for each axis

In addition, to attain a better compromise between performance, disturbance rejection and stability, always respecting a certain limitation of the control signal, 2 degree-of-freedom controllers have been chosen. Each controller acts at the reference and error signals, thus, it has feedforward and feedback components, which

will be calculated simultaneously (using a LMI [1] approach) in order to achieve an optimal solution for the H_∞ problem. This approach is really effective when there are others criteria to respect such as actuator limitation [14].

The structure of the desired controller r decentralized control is detailed in figure 7.1. It is important to underline that the abduction/adduction axis, with which the other two axes do not have relevant interactions, does not present a frequency weighting function for disturbance rejection (W_3).

The synthesis of the SISO controllers is based in the diagonal elements g_{ii}^{θ} (Eq. 6.2) and in the choice of the weighting functions. Until this point, everything is calculated using continuous-time representation (Laplace s-domain), but embedded electronics, in our case the DSPs, require discrete controllers. So, as a final step, the calculated controller will be discretized using the Bilinear (Tustin) transformation with a sampling period $T_s = 1ms$, which is the interval time between two position control loops.

$$s = \frac{2}{T_s}\frac{z-1}{z+1} \tag{7.1}$$

The major advantage of this mapping from s to $z - domain$ with respect to other techniques (notably Forward Euler) is that all the left half s-plane is mapped exactly inside the unitary circle on z-plane. It assures stability on the process of discretization.

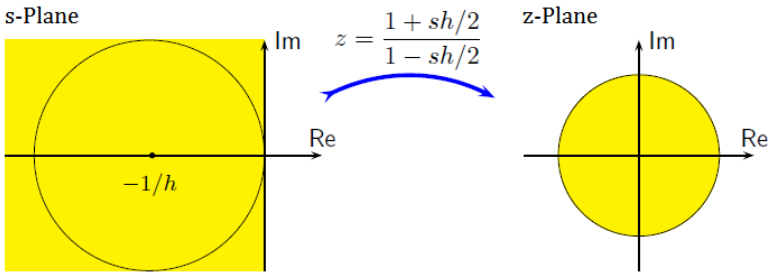

Figure 7.2: Region of stability for Tustin's approximation [36].

Once the z-transfer matrix $K(z^{-1})$ is calculated, the discrete controller is tested with the ZOH correspondent of the plant to assure that we are as nearer of the real conditions as it is possible. Then, when the results are validated on simulation, the C/C++ code is generated either automatically using Matlab Code Generator or manually by implementing the IIR filters directly on the DSP state machine. As $K(z^{-1})$ is at the canonical form, the discrete filters coefficients can be explicitly identified which eases the process.

1. Linear Matrix Inequality

7.1 Standard H_∞ problem

Let $P(s)$ be an axis augmented plant considering one diagonal element of the nominal system presented in equation 6.2 and the weighting functions, i.e $P(s)$ is the transfer function between all inputs and outputs in figure 7.1 if the controller $k_{ii}(s)$ is "deleted" from it.

The standard H_∞ problem consists on finding an optimal value $\gamma > 0$ and a controller $K(s)$ stabilizing the closed-loop in figure 7.3 which could guarantee the following inequality:

$$\left\| \mathcal{F}_l(P(s), K(s)) \right\|_\infty < \gamma \tag{7.2}$$

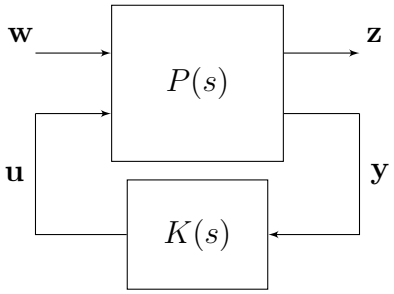

Figure 7.3: Standard H_∞ problem for the case study

where,

$$\mathbf{w} = [\, q_{ref} \;\; d \,]^T \qquad \mathbf{z} = [\, z_1 \;\; z_2 \,]^T$$
$$\mathbf{u} = i_{motor} \qquad \mathbf{y} = [\, \theta_{ref} \;\; e \,]^T$$

As $K(s)$ is a 2 DoF controller, it is interesting to calculate the feedback and feedforward sensitivity transfer functions for the i-th axis:

$$\tilde{S}_{fb} = \frac{1}{1 + \tilde{g}_{ii}^{\theta} \cdot k_{ii}^{fb}} \qquad \tilde{S}_{ff} = \left(1 - \tilde{g}_{ii}^{\theta} \cdot k_{ii}^{fb}\right) \tag{7.3}$$

where $\tilde{S}_{fb}$ is the classical sensitivity transfer function due to feedback part and $\tilde{S}_{ff}$ is the sensitivity function due to feedforward term. Hence, the product $(\tilde{S}_{fb}\ \tilde{S}_{ff})$ is the complete transfer function from the error signal e to the reference θ_{ref}.

Thus, from figure 7.1 and equation 7.3, the system can be written on the following form and using the complementary sensitivity $\tilde{T}_{fb} = 1 - \tilde{S}_{fb}$:

$$\begin{bmatrix} z_1 \\ z_2 \end{bmatrix} = \begin{bmatrix} W_1 \tilde{S}_{fb} \tilde{S}_{ff} T_{ii} & -W_1 \tilde{S}_{fb}\ \tilde{g}_{ii}^{\theta} W_3 \\ W_2 \tilde{S}_{fb} \left(k_{ii}^{ff} + k_{ii}^{fb}\right) T_{ii} & -W_2 \tilde{T}_{fb} W_3 \end{bmatrix} \begin{bmatrix} q_{ref} \\ d \end{bmatrix} \tag{7.4}$$

On equation 7.2 $\mathcal{F}_l$ is the Lower Linear Fractional Transformation defined as the transfer matrix from w to z. Thereby, using equations 7.2, 7.3 and 7.4, the standard H_∞ optimization problem can be rewritten and simplified as follows:

$$\left\| \begin{matrix} W_1 \tilde{S}_{fb} \tilde{S}_{ff} T'_{ii} & -W_1 \tilde{S}_{fb}\, \tilde{g}^{\theta}_{ii} W_3 \\ W_2 \tilde{S}_{fb} \left(k^{ff}_{ii} + k^{fb}_{ii} \right) T'_{ii} & -W_2 \tilde{T}_{fb} W_3 \end{matrix} \right\|_\infty < \gamma \tag{7.5}$$

where T'_{ii} has substituted T_{ii} because the value of q_{ref} should be normalized between 0 (or -1 for abduction axis) and 1 for the controller synthesis using Robust Control MATLAB Toolbox. In fact, all system inputs and outputs should be normalized so that internal variables could have physical values for a coherent controller synthesis. Hence the value of T'_{ii} are important for the correct sizing of the problem and is given as follows.

$$T'_{ii} = T_{ii}\; q^i_{max}$$

$q^i_{max} = \pi/6$ for axis 1 (abduction/adduction movement) and
$q^i_{max} = \pi/2$ for axes 2 and 3 (flexion/extension movements).

This MATLAB Toolbox gives several methods for solving the H_∞ optimization problem such as Standard 2-Riccati equations ($'rci'$), Linear Matrix Inequality ($'lmi'$) or Maximum Entropy solution ($'maxe'$). As we are going to see further on this text, the chosen method was the LMI method because of performance purposes.

7.2 Choice of weighting functions

In this section a first order filter of the following general expression will be considered for the construction of the weighting functions $W_1(s)$ and $W_3(s)$.

$$\frac{1}{W(s)} = \frac{k_{ov} s + \frac{3\varepsilon_{stat}}{T_{rep}}}{s + \frac{3}{T_{rep}}}$$

where,

T_{rep} : response-time to achieve 95% of the steady-state output
k_{ov} : overshoot absolute value (equals 1 if no overshoot)
ε_{stat} : static error

Performance Requirements

The filter $W_1(s)$ is chosen directly from the specifications on the tracking performances (sensitivity function) for dexterous manipulation:

– the tracking movement must not present overshoot
– the T_{rep} response-time must be less than or equal to $0.5s$
– the maximal static error must be lower than 0.1%

Also, in order to normalize output z_1, $W_1(s)$ should present a normalization term of $1/(T'_{ii})$. Finally, the expression for the weighting function imposing performance requirements is:

$$\frac{1}{W_1} = \frac{s+0.006}{s+6}\,T'_{ii} \;\Rightarrow\; W_1 = \underbrace{\frac{s+6}{s+0.006}}_{W'_1}\,\frac{1}{T'_{ii}} \tag{7.6}$$

Disturbance Rejection

To compute $W_3(s)$, which is determinant to avoid the effects of disturbances in reference and control signals, the expression of W'_1, the joint-level RGA and a disturbance transfer function will be used. To better understand the choice of $W_3(s)$, its expression can be written in function of a pure gain and a filter as follows:

$$W_3 = \alpha \times W'_3$$

Primarily, from the joint-level RGA (Fig. 6.2), one may note that the interactions are representative only in low frequencies, which leads us to conclude that a high-pass filter, as well as $1/W_1$, should be employed for disturbance rejection. Then, to calculate the gainα, as there is no representative interaction between abduction/adduction and the other flexion/extension movements, the 2x2 RGA sub-matrix has two identical lines (or columns) as per its properties [37]. Hence, based in a worst case scenario, α is calculated considering the disturbance transfer function whose static gain is the greatest one.

The input disturbance transfer function from axis j to axis i is represented by $g^\theta_{ij}/g^\theta_{ii}$ and the greatest static gain is found in the disturbance transfer function from axis 3 to axis 2:

$$\left.\frac{g^\theta_{23}}{g^\theta_{22}}\right|_{s\to 0} = -0.391$$

So, taking the worst case, when actuator is saturated ($i_3 = 170$ mA), it is trivial to determine W_3's first term:

$$\alpha = -0.391 \cdot 0.170 \approx -0.07$$

At this point, to compute W'_3 we use the fact that the product $W'_1\,W'_3$ determines the dynamics of disturbance rejection on the reference signal. Hence, we infer some

performances:

- the disturbance rejection must not present overshoot
- disturbance rejection must be as fast as the tracking specification
- the maximal static error must be lower than 1%

Therefore,

$$W_1' \cdot W_3' = \frac{s+6}{s+0.06} \;\Rightarrow\; W_3 = -0.07\;\frac{s+0.006}{s+0.06} \tag{7.7}$$

Actuator Limitation and Stability Analysis

The non linearities presented in section 5.3 are indeed additive incertitudes and should be considered to guarantee robust stability as announced by the 1^{st} *condition* using the Small-Gain Theorem [14, 38] for the already presented scheme in figure 7.4. Moreover, as per the 2^{nd} *condition*, in order to respect stability criterion regarding independent design of decentralized controller the complementary sensitivity must respect the following $||\tilde{T}_{fb}||_\infty < 1.28$, as announced in section 6.4

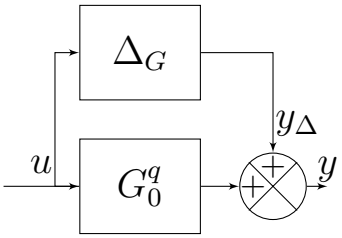

Figure 7.4: Uncertain system represented by additive incertitudes $\Delta(s)$

W_2 is not only a weighting function to guarantee actuator limitations but also, it is implied to ensure the 1^{st} and 2^{nd} *conditions*. To accomplish its first role, a value of W_2 is established so that the motor current is always less than or equal to 170 mA. Then, once the controller calculated, it is checked if this only specification is enough to respect the small-gain theorem and if $||\tilde{T}_{fb}||_\infty < 1.28$, guaranteeing internal stability for the complete system.

$$\frac{1}{W_2} = 0.170 \tag{7.8}$$

Considering all possible $\Delta_G(s)$ realizations and a weighting function $w_a(s)$, for which $\left\|\Delta_G(s)\right\|_\infty \leq \left\|w_a(s)\right\|_\infty$, the small gain theorem infers that for an additive incertitude:

$$\left\|(k_{ii}^{ff} + k_{ii}^{fb})\tilde{S}_{fb}\right\|_\infty < \frac{1}{\left\|w_a(s)\right\|_\infty} \;\Rightarrow\; \left\|(k_{ii}^{ff} + k_{ii}^{fb})\tilde{S}_{fb})\right\|_\infty < \frac{1}{\left\|\Delta(s)\right\|_\infty} \tag{7.9}$$

In figure 7.5, the dashed blue curves represent the weighting functions (W_2^{-1}) for each axis, the red ones represent the inverse of all possible additive uncertainties ($\Delta_G(s)^{-1}$) obtained by the subtraction of all generated uncertain systems by MATLAB Robust Control Toolbox from the nominal model G_0. Finally, the green curves represent all uncertain systems $(k_{ii}^{ff} + k_{ii}^{fb})S_{fb}$ created using the calculated robust controllers and the overall sensibility function.

One can see that the inequality 7.9 is satisfied for all frequency spectrum and that the weighting function W_2 is also respected. Consequently, all systems are stable (ensuring 1^{st} *condition*) and the control signals will never pass 170 mA.

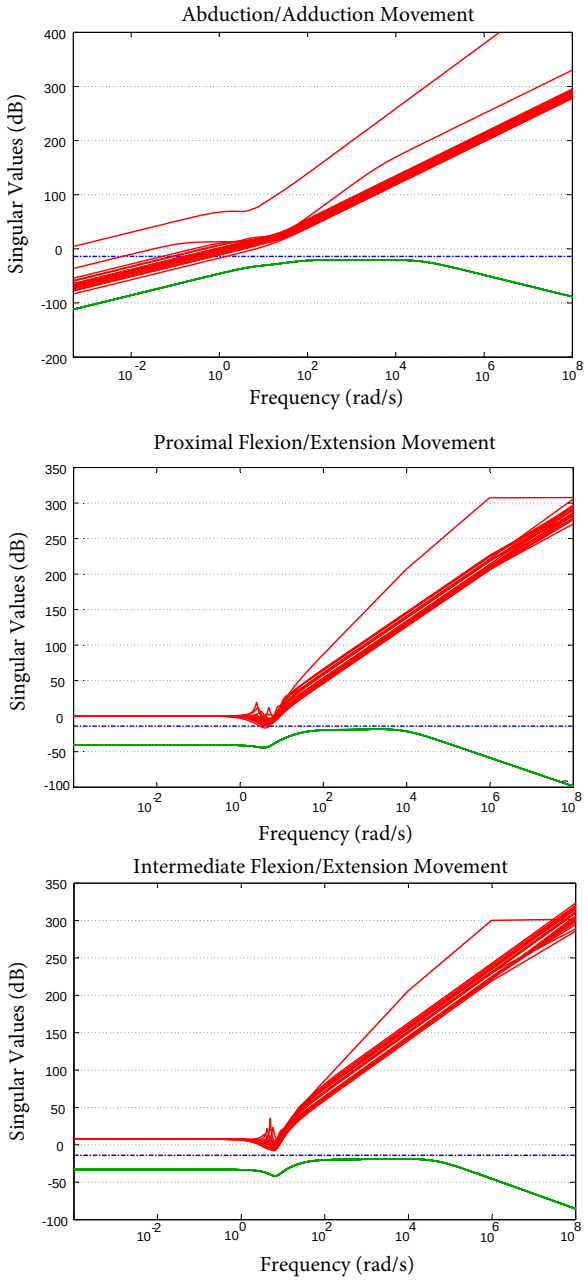

Figure 7.5: Small-gain theorem verification using final controllers

As a last conclusion for stability, $1/(W_2\,W_3)$ weights $||\tilde{T}_{fb}||$. So, using the same principle as before, the value of $||\tilde{T}_{fb}||$ can be computed using the calculated controllers. The results for each axis are detailed in table 7.2 and the value of $||\tilde{T}_{fb}||$ is alway less than $1/\mu(E) = 1.28$, satisfying also the 2^{nd} *condition*. Next section details some important facts for the controller synthesis.

7.3 Controller Synthesis

The final structure of the controller with the uncertain system is represented in figure 7.6 where the feedback and feedforward components of the decentralized controller are in evidence. To solve the H_∞ optimization problem previously stated (Eq. 7.5 and Fig. 7.1), we use the LMI Method considering the weighting functions specified in the last section.

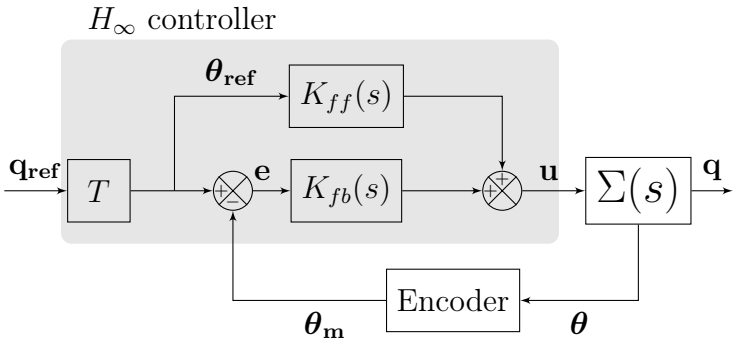

Figure 7.6: Complete control diagram for the multi-variable uncertain system

To do so, once the problem is well posed and all uncertain and nominal transfer functions calculated, basically, three MATLAB Robust Control Toolbox functions are used as depicted on the following part of the code:

```
% Augmented System calculation
[A,B,C,D] = linmod('AugmentedPlant') ;
P         = minreal(ss(A,B,C,D));

% Calculation of the SISO H_infinity controller
[K,~,GAMMA,~] = hinfsyn(P,2,1,'METHOD','lmi');
```

The first function (*linmod*) calculates a realization of the Augmented Plant, considering the system and weighting functions. Nevertheless, this realization is normally too complex and not minimal, for that purpose, the function *minreal* is used to determine a simpler and minimal augmented plant P. Finally, as the optimization problem is already posed, the function $hinfsyn$ is used to solve the problem using the LMI method. This function returns the 2 DoF controller ($k_{ii} = [k_{ii}^{ff} \quad k_{ii}^{fb}]$) for each axis and the correspondent γ.

Once again, the transfer function for both feedback and feedforward controllers are usually not minimal, with high order numerators and denominators. Hence, a final step of careful model reduction is carried out in order to simplify at most the controllers. The values of γ for the optimization processes are shown on table 7.1.

Table 7.1: H_∞ optimization solution

Axis	γ
Abduction (q_1)	1.1089
1^{st} flexion (q_2)	1.1611
2^{nd} flexion (q_3)	1.1595

One may note that the result for axis 1 is slightly better than the others, this is due to the fact that it was not necessary to consider disturbance rejection for this axis and so the optimization is a little easier. Nevertheless, all three γ's are close to one, this means that all weighting functions were respected reasonably well and that the requirements stated in time-domain were achieved. The final multi-variable controllers have the following transfer functions:

$$K_{ff} = \begin{pmatrix} k_{11}^{ff} & 0 & 0 \\ 0 & k_{22}^{ff} & 0 \\ 0 & 0 & k_{33}^{ff} \end{pmatrix} \qquad K_{fb} = \begin{pmatrix} k_{11}^{fb} & 0 & 0 \\ 0 & k_{22}^{fb} & 0 \\ 0 & 0 & k_{33}^{fb} \end{pmatrix} \tag{7.10}$$

$$\begin{aligned} k_{11}^{ff} &= \frac{-4825.3(s+19.48)}{(s+4.046\cdot 10^4)(s+490.9)} & k_{11}^{fb} &= \frac{4886.9\ (s+19.47)(s+5.349)}{s(s+4.046\cdot 10^4)(s+490.9)} \\ k_{22}^{ff} &= \frac{-1.0066\cdot 10^5(s+40.34)}{(s+8908)(s+2897)} & k_{22}^{fb} &= \frac{1.0067\cdot 10^5\ (s+34.52)(s+6.051)}{s(s+8908)(s+2897)} \\ k_{33}^{ff} &= \frac{-3.5819\cdot 10^5(s+39.41)}{(s+4.59\cdot 10^4)(s+2287)} & k_{33}^{fb} &= \frac{3.5824\cdot 10^5\ (s+33.55)(s+6.129)}{s(s+4.59\cdot 10^4)(s+2287)} \end{aligned}$$

All controllers have been reduced to a minimal form without losing efficiency. In addition, in order to achieve $\varepsilon_{stat} = 0$ for both tracking performance and disturbance rejection an integrator was evidenced on each feedback controller. This fact does not compromise the system stability as we can see figure 7.5, on which the controllers in equation 7.10 were used to build the curves.

Table 7.2: SISO H_∞ design for the three axes unit.

Axis	Gain Margin	Phase margin	$\|\|\tilde{T}\|\|_\infty$	$\|\|\tilde{S}\|\|_\infty$
Abduction (q_1)	56 dB	78°	1.07	1.09
1^{st} flexion (q_2)	22 dB	66°	1.04	1.30
2^{nd} flexion (q_3)	35 dB	68°	1.03	1.24

Finally, the bilinear transformation (Eq. 7.1) is applied and the discrete filters are calculated to be implemented on the DSP. In addition to the respect of stability *conditions*, design results are summarized in table 7.2, where the exposed stability gain and phase margins can be considered as very satisfactory.

The last part of this document will bring some of the acquired performance results on the real robot system using the calculated H_∞ controllers. Then, the final considerations about the whole project are stated, bringing also some future perspectives and improvements for this work.

Part III

H_∞ Controller Results and Final Considerations

Chapter 8

Results of the Experiment

Once all controllers have been calculated and tuned, it is time to test the system's performances using the H_∞ embedded position controller. This chapter is devoted to the presentation and analysis of such results at the motor-level (section 8.1) and then at the joint-level (section 8.2), which is the real objective to be achieved. At the end of the chapter a brief evaluation of the experimental performances is done.

8.1 Motor-Level Experiment

As a first result, it can be seen in figure 8.1 that the performance requirements have been achieved, independently, for all three axes at the motor level. On that case, there are no simultaneous movements, each axis has been moved at a time.

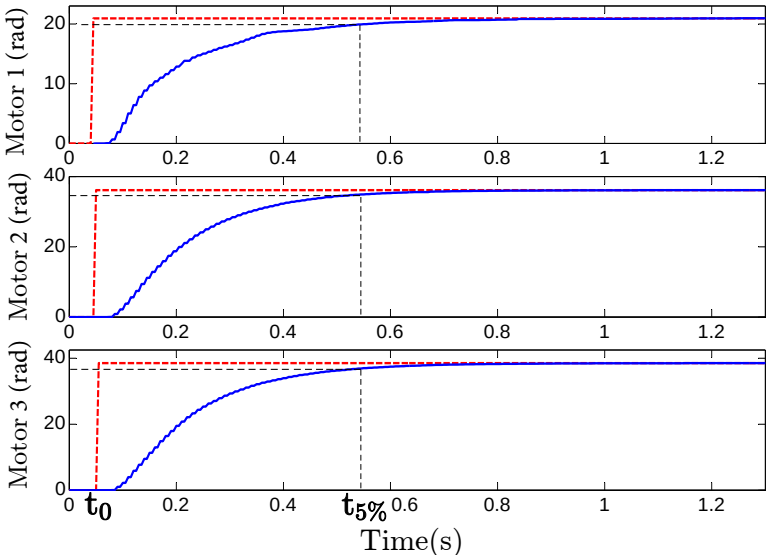

Figure 8.1: Step response for each axis

The values of t_0 and $t_{5\%}$ indicate, respectively, the reference step start and the system's 5% response moments. For all three axes, t_0 was the same and it is

interesting to underline that they have the same bandwidth since the analog filters (W_1') were the same for the synthesis of all axes' controllers.

From figure 8.1, $t_0 = 50ms$ and $t_{5\%} = 550ms$, which means a 5% response-time of $\Delta T_{5\%} = 500ms$ as wanted. Indeed, there is also a dead zone due to communication latency of the set-point sending from the host-PC (Matlab) to the DSP. So, $\Delta T_{lat} = 25ms$ and as it is added to the response-time and it is not taken into account for the controller synthesis, it could be inferred that the mechanical 5 % response-time is $\Delta T_{5\%} = 475\ ms$.

One should also observe that there is no overshoot and that the movement is very smooth due to the choice of the appropriate weighting functions W_i.

8.2 Joint-Level Experiment

Even though the analysis at the motor level is necessary it is not sufficient by itself. In order to better visualize the system's response and to analyze the effects of coupling, all articular angles should be directly measure, so, to accomplish that, three potentiometers as shown in figure 8.2 have mounted on the 3-axes unit for tests purposes.

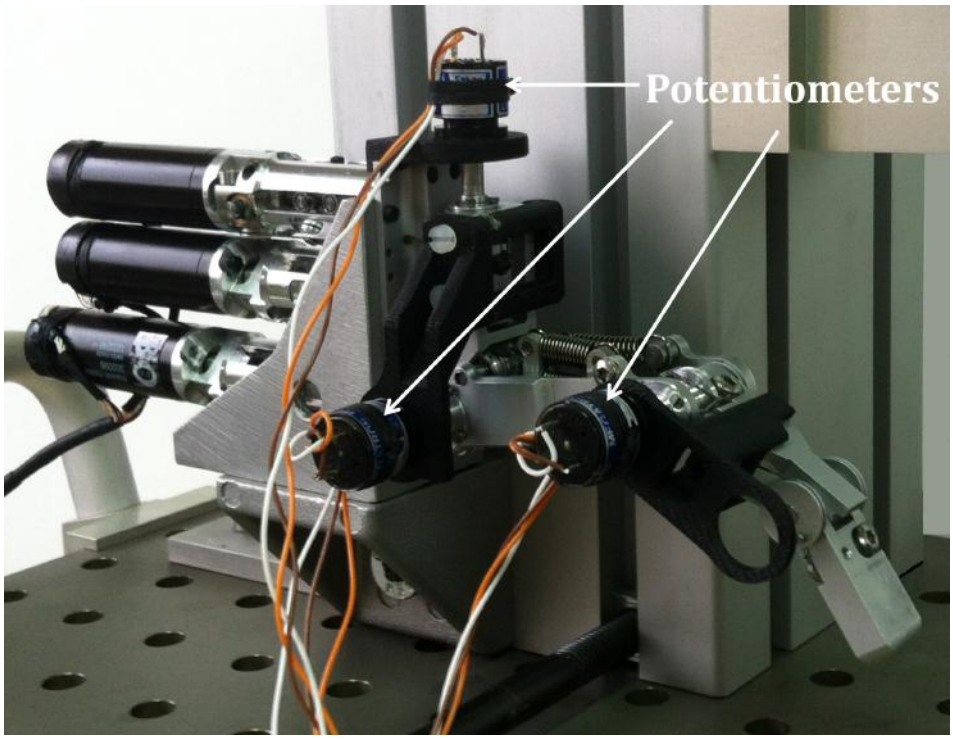

Figure 8.2: Test bench

With such test bench two kinds of experiments are performed:

(i) A sequence of joint steps exploring all possible interactions;

(ii) Time-shifted sinusoidal tracking of joint references with variable amplitudes.

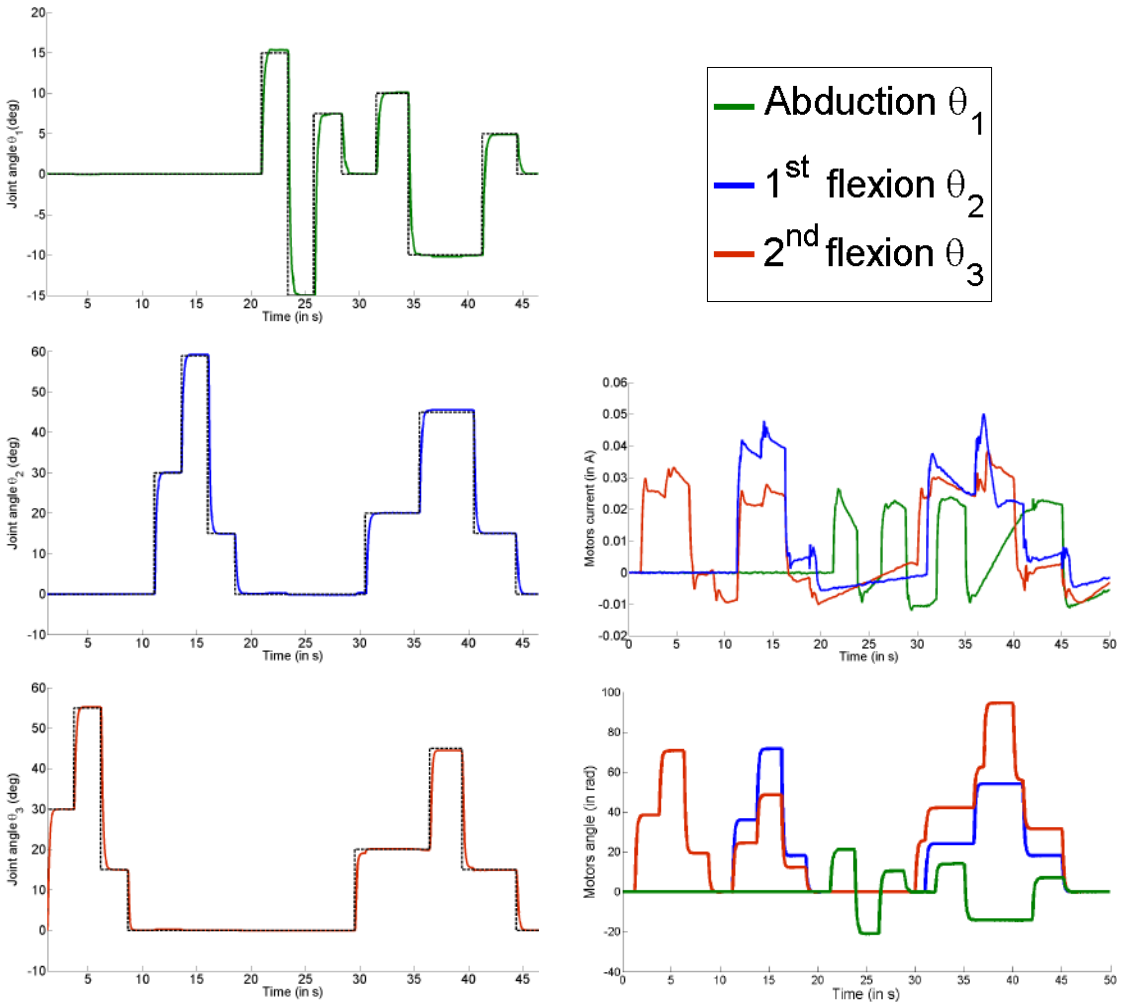

(a) Joint-side positions q in the tracking experiment and references (dashed lines).

(b) Motor current and measured motor-side positions θ in the tracking experiment.

Figure 8.3: Sequence of steps with simultaneous axes movements

At the first experiment, figures 8.3a and 8.3b show, for each axis, the evolution of the motor angle in radians, the articular angle in degrees and the motor current in mA for a given sequence of steps.The objective of this experiment is to show that even in the presence of simultaneous movements, each axis is capable to achieve the given joint set-points with the same performances presented in figure 8.1, rejecting the influence of the other two axes at the same time.

Considering the motor angles, figure 8.3b (bottom) shows the displacements of the motor shaft in order to accomplish the tracking on joint-side via the transformation matrix T. One might note that the second flexion/extension motor moves also when the first one moves in order to maintain the tendon tensioned as explained before. In figure 8.3a, the black dashed lines represent the ideal joint angle, calculated from the measured motor angles by the transformation matrix T^{-1}, to track perfectly the input joint signal and the filled lines are the angles measured by the potentiometers. As the mechanism is not perfect, there is some

backlash at the motor-to-joint transmission and this fact yields to static errors in the articular tracking. However, these errors are really small and they not represent a significant lost of performance for the envisaged applications. The greatest absolute static errors for each axis are presented in table 8.1.

Table 8.1: Maximum static error for each axis

Axis	$\|\varepsilon_{stat}\|_{Max}$
Abduction (q_1)	0.2^o
1^{st} flexion (q_2)	0.6^o
2^{nd} flexion (q_3)	0.6^o

In figure 8.3b (top) it is shown the current in each motor and we see that they are coherent control signals and distant from the actuator saturation even if great displacements are done. Extreme tests were also performed considering maximal joint angles and the control signal has never passed $170mA$

The second and last experiment consists in the application of simultaneous sines to each axis. Nevertheless, the amplitude of this sines are different, they have great amplitudes shifted in time. So, it is a way to prove that we can realize decoupling by the controller, i.e. even if other axes have great amplitudes a certain axis can track totally different reference signals at the same time.

In figures of 8.5 the red dashed lines represent the articular reference signal and the blue lines are the potentiometers measures for each axis. From these figures, it becomes clear that the disturbance rejection works properly because each axis is able to track its own reference independently of the others.

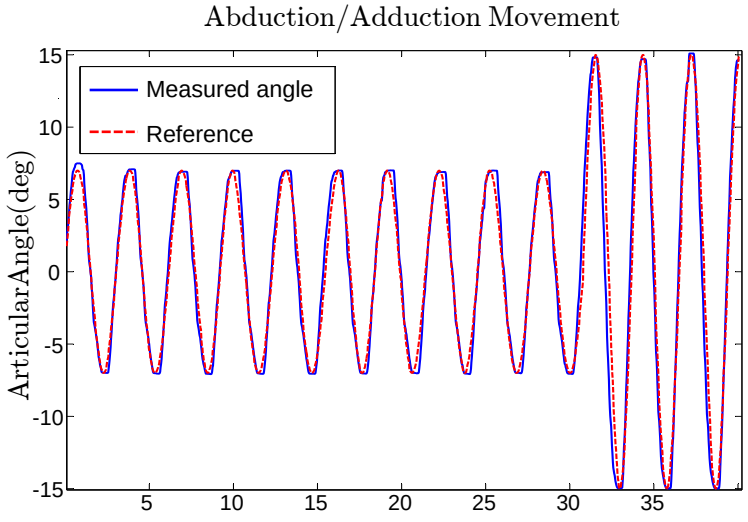

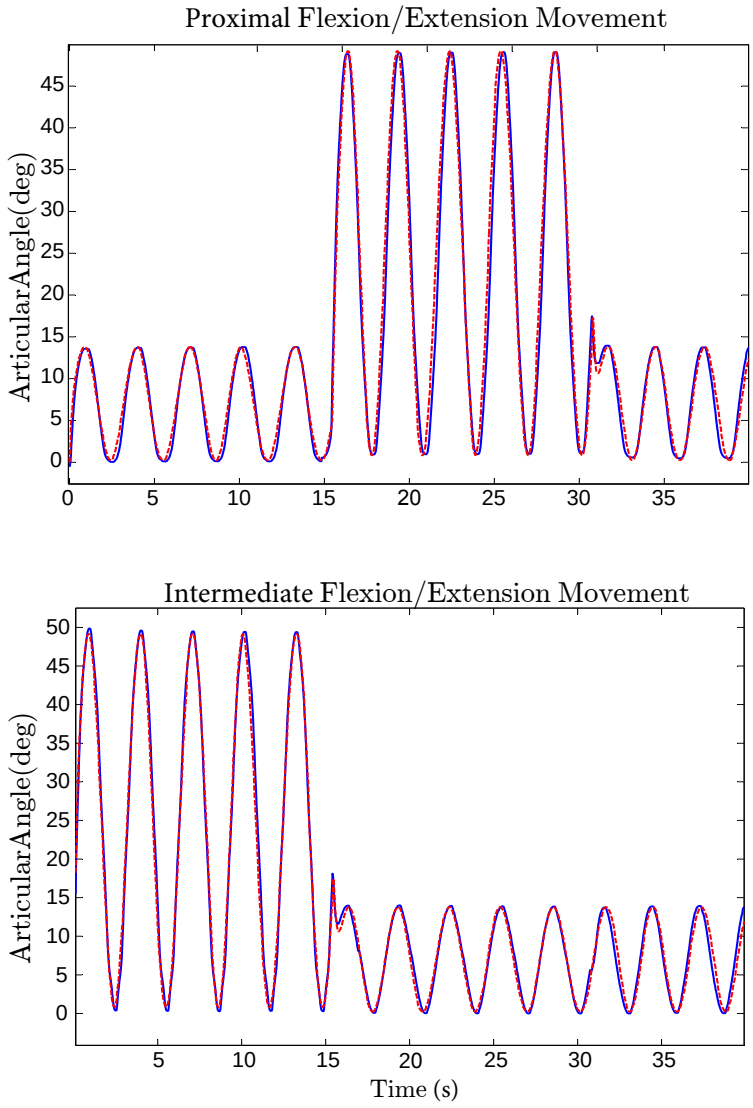

Figure 8.5: Sinusoidal joint references with different amplitudes and applied at different moments for the three axes.

8.3 Experimental performances evaluation

The proposed control approach has been evaluated on a 3 Axes Unit for which extra position sensors have been temporarily mounted on each axis unit joint. Time-responses are very smooth and do not exhibit any overshoot. According to controller specifications, no saturation have been observed for the control (Fig. 8.3b top) and disturbances related to axes coupling are well rejected at motor control current and motor-side position levels.

Chapter 9

Final Considerations

The design rationale of the dexterous CEA hand relies on the combination of two main pillars: modularity and backdrivability. Modularity is achieved by the design and optimization of a separable sub-assembly, the *3 axes unit*, which is then integrated in all fingers and the thumb. Backdrivability is addressed at both actuator and transmission level. Motor output and ball-screw reduction ratio are chosen to simultaneously obtain a sufficient actuator output and a minimum acceleration-dependent backdrivability. For the mechanical transmission a new design is presented which minimizes the number of idle pulleys and direction changes in the tendon routing, minimizing friction-dependent backdrivability and providing system decoupling which is very important to facilitate controllers design. Thus, the mechanical advantages of the proposed design have a direct impact in the controllability of the mechanism, which in turn enhances the dexterity of the hand.

9.1 Conclusions

The first part of this project was principally related to perform position and force experiments for a finger. With respect to the position experiments, the decoupled axes of the 3 axes unit were validated experimentally. Then, onto torque ones, the backdrivable mechanism was explored to develop an algorithm to estimate external contact forces in the distal phalanx.

Furthermore, if the contact point could be located by an additional sensing technology, it is possible to obtain an estimate of the contact forces. This feature enhances the dexterity related to the sensory apparatus of the hand: every surface becomes sensitive as every part of the hand is driven by a backdrivable actuator. Let us note that the proposed approach only requires the contact point information from a complementary additional sensing technology. This could be provided by a tactile skin with only good spatial resolution (even with limited or inexistent

force sensitivity). In addition, backdrivability also opens new possibilities for compliance control, which improves stability of a multi-fingered grasp against external disturbances of unknown intensity.

From this first part of the project, I believe that my professional skills on mechatronics were considerably improved. In order to perform the tasks and to make progress within the project, I have been confronted with several problems in electronics (specially for the conception of an ADC circuitry compatible with the DSPs), mechanics (for the system's comprehension and reparation) and computer science (for the DSP's programming and data acquisition). Despite being more practical, this first moment was also important to give me a prime contact with Robotics Modeling and Control whose results were published in an IEEE scientific conference [39].

The second part of the project was more theoretical than the first one and I had the opportunity to deepen my knowledge on robust control theory - focusing in the H_∞ synthesis - applied to a very interesting case. Fortunately, the expected results were achieved and we could once again publish our results, but that time, on an IEEE scientific journal [40]. Even tough this part was less practical, in order to implement the final controllers and to perform the experiments leading to the final results, the background of the first months was once again more than necessary.

Thanks to modularity and axes decoupling, three high performance robust controllers have been developed for each finger of the CEA hand. The performances achieved with the optimized controllers designed to our specific problem were way better than the ones reached with the classical proportional-derivative controllers already implemented. In addition, stability is always ensured with the new controllers.

Finally, the technical background and the experiences acquired during this project - working with such a complex system - were essential to increase my professional maturity and also to develop R&D capabilities in this area. I believe this work fits quite well an Undergraduate Project because it includes, at the same time, a well-founded research and the various elements I studied during the course of Automation and Control Engineering. I had the opportunity to develop classic and modern closed-loop digital control laws, to use the dynamic model of a robot in order to estimate a contact force with an object, to program DSPs, to enter in some details of Industrial Networks for Control and Automation, to repair and analyze electronic boards and mechanical systems. Hence, as per its multidisciplinary characteristic, this project was a necessary final element to accomplish this first step on my professional career: to become an Automation and Control Engineer.

9.2 Future Perspectives

As future perspectives of this project the following points can be listed:

- Extend the force estimation technique to an online algorithm in order to adapt the grasp and force applied by the fingers depending on the kind of manipulated object;
- Explore backdrivability for compliance control, which improves stability of a multifingered grasp against external disturbances of unknown sources;
- Migrate to a complete real-time system, considering a better user interface (using ROS for example) integrated to a hard RTOS (i.e. VxWorks, Xenomai, QNX, etc) and communicating in a real-time network.

Since this project has been done in France, during an internship, it is difficult to give it a real line of continuation but these points here-above are some of the ones that could be improved in order to achieve better and more interesting results.

Bibliography

[1] R. O. Ambrose, H. Aldridge, R. S. Askew, R. R. Burridge, W. Bluethmann, M. Diftler, C. Lovchik, D. Magruder, and F. Rehnmark, "Robonaut: Nasa's space humanoid," *IEEE Intell. Syst.*, no. 1, pp. 57–63, 2000.

[2] Albu-Schaffer, A., Haddadin, S., Ott, Ch, Stemmer, A., Wimbock, T., Hirzinger, and G., "The DLR lightweight robot: design and control concepts for robots in human environments," *Industrial Robot: An International Journal*, vol. 34, no. 5, pp. 376–385, 2007.

[3] H. Kawasaki, T. Komatsu, and K. Uchiyama, "Dexterous anthropomorphic robot hand with distributed tactile sensor: Gifu hand ii," *IEEE/ASME Trans. Mechatron.*, vol. 7, no. 3, pp. 296–303, 2002.

[4] H. Liu, K. Wu, P. Meusel, N. Seitz, G. Hirzinger, M. H. Jin, Y. W. Liu, S. W. Fan, T. Lan, and Z. P. Chen, "Multisensory five-finger dexterous hand: The DLR/HIT Hand II," in *Proceedings of the IEEE/RSJ International Conference on Intelligent Robots and Systems*, 2008, pp. 3692–3697. [Online]. Available: http://dx.doi.org/10.1109/iros.2008.4650624

[5] L. Jones and S. Lederman, *Human Hand Function*. Oxford University Press, USA, 2006. [Online]. Available: https://books.google.com.br/books?id=NRI8n9oeAsUC

[6] H. E. Wheat, L. M. Salo, and A. W. Goodwin, "Human ability to scale and discriminate forces typical of those occurring during grasp and manipulation," *The Journal of neuroscience*, vol. 24, no. 13, pp. 3394–3401, 2004.

[7] L. Biagiotti, F. Lotti, C. Melchiorri, and G. Vassura, "How far is the human hand? a review on anthropomorphic robotic end-effectors," in *University of Bologna, Tech. Rep.*, 2004.

[8] C. Melchiorri and M. Kaneko, "Robot hands," in *Springer Handbook of Robotics*. Springer-Verlag, 2008, ch. 14, pp. 345–360.

[9] A. Bicchi, "Hands for dexterous manipulation and robust grasping: A difficult road toward simplicity," *IEEE Transactions on Robotics and Automation*, vol. 16, no. 6, pp. 652–662, 2000.

[10] L. N. R. Reis, "Modeling and Kinematic Control of a Robotic Hand," 2012, undergraduate Project, Automation and Control Engineering, POLI-UFRJ.

[11] Z. Su, J. A. Fishel, T. Yamamoto, and G. E. Loeb, "Use of tactile feedback to control exploratory movements to characterize object compliance," *Frontiers in neurorobotics*, vol. 6, 2012.

[12] CEA. (2012) Video about the cea hand inside handle project and some use cases. [Online]. Available: http://www.youtube.com/watch?v=KF6pzc1nBl0

[13] W. Khalil and É. Dombre, *Modélisation, identification et commande des robots*, ser. Collection robotique. Hermes Science Publications, 1999. [Online]. Available: http://books.google.com.br/books?id=xNi8AAAACAAJ

[14] G. Scolertti and V. Fromion. (2007) Introduction à la commande multivariable des systèmes : méthodes de synthèse fréquentielle H_∞. [Online]. Available: https://magarotto.users.greyc.fr/pdf/CM_CommRob_2007.pdf

[15] J. Martin, B. Huard, M. Robert, and M. Grossard, "Design of a novel self-sensing and compliance controlled robotic finger joint," in *IEEE/ASME International Conference on Advanced Intelligent Mechatronics*, 2011, pp. 1520–1532.

[16] J. Martin and M. Grossard, "Design of a fully modular and backdriveabe dexterous hand," in *Submitted to International Journal of Robotics Research*, 2013.

[17] ShadowRobotCompany. (2013) Shadow dexterous hand technical specifications. [Online]. Available: http://www.shadowrobot.com

[18] K. Koganezawa, N. Kunugi, and R. Niikura, "Backdrivable mechanism for artificial finger," in *18th IFAC World Congress*, 2011, pp. 8095–8100.

[19] Nakamura Lab., "The Development of actuators with Backdrivability," 2014. [Online]. Available: https:/http://www.ynl.t.u-tokyo.ac.jp/research/backdrive/index.php

[20] R. M. Murray, Z. Li, and S. S. Sastry, "A mathematical introduction to robotic manipulation," 1994.

[21] National Instruments, "Control Loops in a Motion Controller and Drive Electronics for a Brushed DC Motor," 2014. [Online]. Available: http://www.ni.com/white-paper/3195/en/

[22] P. Hamon, M. Gautier, P. Garrec, and A. Janot, "Dynamic Identification of Robot with a Load-Dependent Joint Friction Mode," in *International Conference on Robotics, Automation and Mechatronics*, Singapour, Singapore, Jun. 2010, pp. pp. 129–135. [Online]. Available: https://hal.archives-ouvertes.fr/hal-00583164

[23] A. C. Bittencourt, E. Wernholt, S. Sander-Tavallaey, and T. Brogardh, "An extended friction model to capture load and temperature effect in robot joint," in *Proceedings of the IEEE/RSJ International Conference on Intelligent Robots and Systems*, 2010, pp. 6161–6167.

[24] T. Tuttle and W. Seering, "A nonlinear model of a harmonic drive gear transmission," *Robotics and Automation, IEEE Transactions on*, vol. 12, no. 3, pp. 368–374, 1996.

[25] G. P. Starr, "An experimental investigation of object stiffness control using a multifingered hand," *Robotics and Autonomous Systems*, vol. 10, no. 1, pp. 33 – 42, 1992.

[26] G. Palli and C. Melchiorri, "Model and control of tendon-sheath transmission systems," in *Robotics and Automation, Proceedings 2006 IEEE International Conference on*, May 2006, pp. 988–993.

[27] H. Liu, P. Meusel, J. Butterfass, and G. Hirzinger, "Dlr's multisensory articulated hand. ii. the parallel torque/position control system," in *Robotics and Automation, 1998. Proceedings. 1998 IEEE International Conference on*, vol. 3, May 1998, pp. 2087–2093.

[28] R. V. Dwivedula and P. P. R., "Effect of compliance and backlash on the output speed of a mechanical transmission system," *Journal of dynamic systems, measurement, and control*, vol. 134, no. 3, pp. 33 – 42, 2012.

[29] J. Cruz-Hernandez and V. Hayward, "Phase control approach to hysteresis reduction," *Control Systems Technology, IEEE Transactions on*, vol. 9, no. 1, pp. 17–26, Jan 2001.

[30] Q. Chen, W. Chen, R. Liu, and J. Zhang, "Error analysis and flexibility compensation of a cable-driven humanoid-arm manipulator," in *Robotics and Automation (ICRA), 2011 IEEE International Conference on*, May 2011, pp. 988–993.

[31] M. Grossard, N. Chaillet, and S. Régnier, *Flexible Robotics: Applications to Multiscale Manipulations*. Wiley, 2013.

[32] K. Zhou, J. Doyle, and K. Glover, *Robust and Optimal Control*. Prentice Hall PTR, 1996.

[33] E. Bristol, "On a new measure of interaction for multivariable process control," *Automatic Control, IEEE Transactions on*, vol. 11, no. 1, pp. 133–134, 1966.

[34] S. Skogestad and I. Postlethwaite, *Multivariable Feedback Control: Analysis and Design*. John Wiley & Sons, 1996.

[35] P. Grosdidier and M. Morari, "Interaction measures for systems under decentralized control," *Automatica*, vol. 22, no. 3, pp. 309 – 319, 1986.

[36] Ramon Romankevicius Costa, "COE480 - Controle em Tempo Real," 2014. [Online]. Available: https://moodle.pee.ufrj.br/file.php/15/Slides_do_curso/slides-COE-480.pdf

[37] S. Skogestad and I. Postlethwaite, *Multivariable feedback control: analysis and design*. John Wiley, 2005.

[38] P. Apkarian. (2011) Éléments de la Théorie de la Commande Robuste. [Online]. Available: http://pierre.apkarian.free.fr/COURS/polysae.pdf

[39] M. Grossard, G. Felippe, G. Hamon, and J. Martin, "Force sensing strategy for the backdrivable and dexterous cea hand," in *Advanced Robotics (ICAR), 2013 16th International Conference on*, Nov 2013, pp. 1–7.

[40] M. Grossard, J. Martin, and G. F. d. C. Pacheco, "Control-oriented design and robust decentralized control of the cea dexterous robot hand," *Mechatronics, IEEE/ASME Transactions on*, vol. PP, no. 99, pp. 1–13, 2014.